Materials Advances

REVIEW

View Article Online
View Journal

Check for updates

Cite this: DOI: 10.1039/d6ma00281a

ZIF-67-based hybrid frameworks as high-performance photocatalysts for simultaneous energy conversion and pollutant degradation

Monalisa Samal,[a] Dharitri Rath [b] and Binita Nanda*[a]

Received 28th February 2026,
Accepted 9th April 2026

DOI: 10.1039/d6ma00281a

rsc.li/materials-advances

Amid global escalating environmental challenges, including the dependence on fossil fuels and increasing water contamination, the development of innovative and sustainable technologies has become imperative. Metal–organic frameworks (MOFs), especially ZIF-67 and its derivatives, have emerged as highly versatile materials due to their distinctive structural characteristics, including large surface areas, open crystalline frameworks, and tuneable porosity. A wide variety of synthetic routes and advanced preparation method have been employed to fabricate ZIF-67, leading to a substantial and growing body of literature on its synthesis. This review provides a comprehensive assessment of ZIF-67 synthesis strategies, integrating recent advances and critically analysing the factors governing its morphological and structural features. It further highlights various process optimization approaches developed for the efficient synthesis of ZIF-67. This review offers a comprehensive assessment of ZIF-67-based photocatalysts, detailing their synthetic strategies, structural attributes, and applications in solar-driven hydrogen evolution, hydrogen peroxide formation, CO_2 reduction, and the degradation of dye and pharmaceutical pollutants. ZIF-67 composites show enormous promise for providing environmentally friendly energy solutions and sustainable global solutions, but more thorough research is necessary to fully realize their potential.

1. Introduction

The 21st century faces critical challenges related to energy and water scarcity, driven by rapid population growth, industrialization and heavy reliance on fossil fuels, which has led to severe environmental pollution and rising carbon emissions.[1–3] Over 1.2 billion people still lack access to clean drinking water, while water bodies are increasingly contaminated by agricultural and industrial pollutants.[4–7] Reactive oxygen species (ROSs), which are produced by charge carriers, are essential for the breakdown of both organic and inorganic contaminants and for the transformation of CO_2 into hydrocarbon fuels.[8,9] Semiconductor-based heterogeneous photocatalysis powered by artificial or direct sunlight has been thoroughly studied utilizing materials such as g-C_3N_5,[10,11] perovskites,[12] quantum dots,[13] TiO_2,[14] Bi_2WO_6,[15] CuO,[16] ZnO,[17] CdS,[18] ZnS,[19] and Fe_3O_4.[20] However, issues including wide band gaps, quick recombination of charge-carrier pairs produced by photolysis, photocorrosion, low recyclability, and restricted solar energy use limit the photocatalytic efficacy of these applications.[21,22] Therefore, creating innovative photocatalysts with a wide range of applications is crucial.

In recent decades, MOFs have become important microporous crystalline materials of the coordination polymer family, and their huge surface area, high porosity, and flexible structural design have made them extremely promising for photocatalysis in recent years.[23] These are formed by connecting inorganic metal clusters with organic linkers to form micro or nanoporous structures in one, two, or three dimensions. These materials are very appealing for use in gas storage and separation, energy storage in supercapacitors and batteries, catalysis, and other fields because of their well-developed porosity and adjustable architectures.[24,25] This adaptability in potential applications is due to their topology, ordered porosity, abundant active sites, compositional diversity, high specific surface areas, diverse capabilities and tuneable chemical properties.[26] In work done by Professor Omar M. Yaghi and his colleagues, the term ''metal–organic framework'' was initially used to describe the overall composition (metal ion and organic linker), even though coordination networks were already documented in the early 1900s (Fig. 1).[27] MOFs have attracted significant attention across a wide range of fields due

---

[a] Department of Chemistry, Faculty of Engineering and Technology (ITER), Siksha O Anusandhan (Deemed to be) University, Bhubaneswar, Odisha, 751 030, India. E-mail: binitananda@soa.ac

[b] Department of Chemical Engineering, Indian Institute of Technology Jammu (IIT), Jagti, Jammu – 181 221, Jammu and Kashmir, India

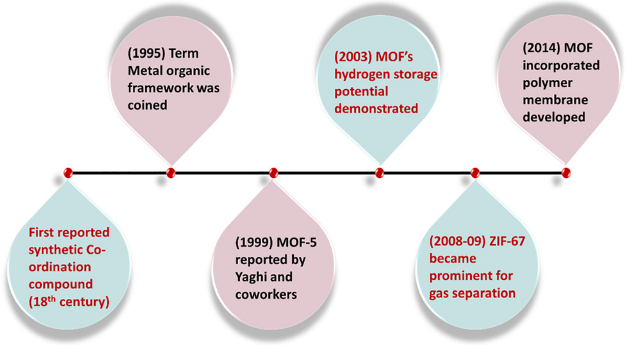

Fig. 1 Timeline showing the development of coordination chemistry leading to the creation of metal–organic frameworks.

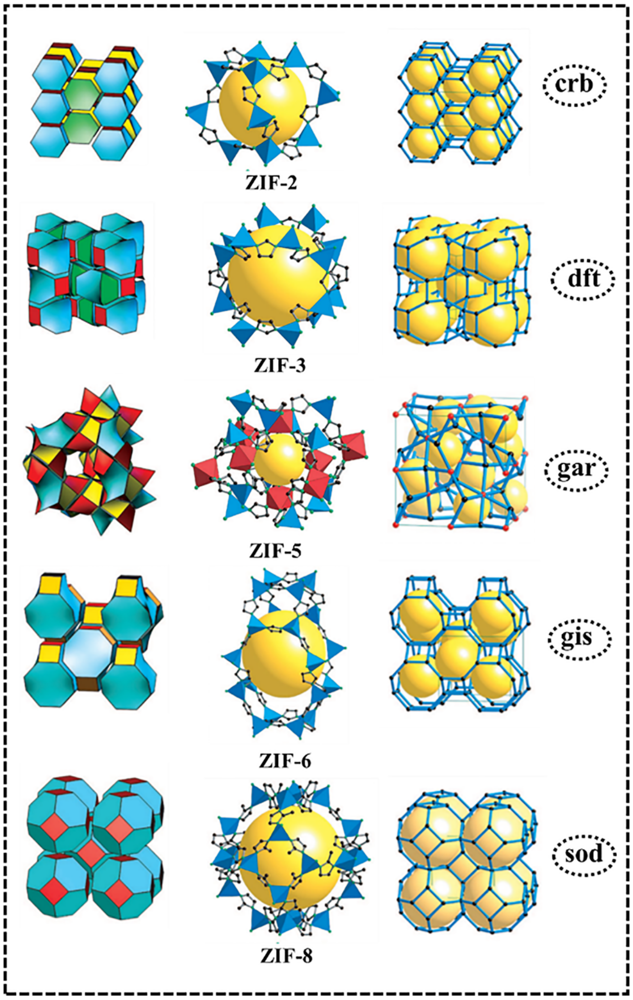

Fig. 2 ZIF single-crystal XRD structures, along with the matching net frameworks; adapted with permission from ref. 38 © 2006 by the National Academy of Sciences of the USA.

to their unique structures and tuneable properties, including applications in photocatalysis, adsorption, renewable energy generation, electronics, energy storage, and biomedicine.[28–30] The large surface area of MOF-templated photocatalysts is especially appreciated because it improves charge-carrier transit, mass transfer, and active-site exposure.[31–33] Apart from their enormous surface areas, ordered pore architectures, and crystalline frameworks, MOFs also provide polymetallic sites and are ideal for integrating with polymers.[34] Their inherent structural characteristics make functionalization simple and affordable, which makes them an excellent material for adsorption and photocatalysis applications across many fields.[35]

Zeolitic imidazolate frameworks (ZIFs) represent a distinctive subclass of porous metal organic frameworks (MOFs), consisting of tetrahedrally coordinated metal cations (M = Zn or Co) interconnected by imidazolate (Im) linkers.[36,37] ZIFs exhibit an M–Im–M bond angle of approximately 145°, closely resembling the Si–O–Si angle in conventional zeolites, which underpins the formation of zeolite-type tetrahedral topologies in a wide range of ZIF structures.[38] Compared with conventional zeolites, MOFs, or their simple physical mixtures, ZIFs offer distinct scientific and technological advantages by synergistically integrating the merits of both material classes, including high surface area, permanent porosity, excellent thermal and chemical stability, and abundant active sites. In their first report, Yaghi *et al.*[38] synthesized 12 ZIFs (ZIF-1 to ZIF-12) by copolymerizing Zn or Co with imidazolate-type linkers. They also examined the thermal and chemical stability of two ZIFs, ZIF-8 and ZIF-11, as well as their gas-adsorption capabilities. All ZIFs synthesized and reported to date can be broadly classified into several distinct network topologies, some of which resemble traditional zeolite frameworks, such as ana, sod, and rho, while others, including dia, correspond to non-zeolitic dense network structures.[39] Owing to these advantages, ZIFs have garnered considerable research interest across a broad range of applications, including gas storage, adsorption, drug delivery, sensing, bioimaging, supercapacitors, and catalysis.[40] A number of representative ZIFs with various network topologies are shown in Fig. 2, demonstrating their various geometries and framework configurations. Furthermore, ZIFs have exceptional chemical and thermal stability, a monodisperse microporous design, and good energetic performance.[41–43]

To date, over 150 ZIF structures have been reported, with a significant number demonstrating strong potential for diverse research and application-oriented studies. ZIF-67 ($Co(Hmim)_2$, where Hmim = 2-methylimidazole), a representative ZIF material, consists of Co^{2+} centres coordinated by 2-methylimidazolate ligands, and it crystallizes in a cubic structure with unit cell parameters $a = b = c = 16.9589$ Å.[40,44] This material is a cobalt-containing zeolitic imidazolate framework composed of tetrahedrally coordinated Co^{2+} centres linked by 2-methylimidazolate ligands, forming a 3D porous structure. Notably, ZIF-67 is isostructural with ZIF-8, sharing the same sodalite (SOD) topology and crystallographic framework, with the metal centre being the primary distinction, where Co^{2+} in ZIF-67 replaces Zn^{2+} in ZIF-8.[45] The imidazolate linker acts as a rigid bidentate bridge, mimicking the Si–O–Si angles in zeolites, which results in a thermodynamically stable SOD topology. This robust metal–ligand bonding endows ZIF-67 with exceptional resistance to framework collapse in organic solvents and under alkaline conditions, where the Co–N bonds remain largely intact. Thermally, the framework remains stable up to 350–400 °C, beyond which ligand decomposition initiates structural breakdown.[46] Notably, ZIF-67 exhibits a high specific surface area ($S_{\mathrm{BET}} > 1700\ \mathrm{m}^2\ \mathrm{g}^{-1}$),[47] providing abundant accessible active sites, while its well-defined micropores ($\sim$0.34 nm pore size) promote reaction processes through strong affinity toward guest molecules.[48,49] It has been demonstrated that pristine ZIF-67 consists of fully tetrahedrally coordinated Co^{2+} centres; therefore, its reactivity toward guest molecules, such as ammonia borane, arises primarily from surface accessible sites, defects, or framework-derived features rather than intrinsic coordinatively unsaturated metal sites.[50,51] ZIF-67-derived metal oxides and metal carbon composites possess unique functionalities absent in the original framework, thereby broadening their application potential. These advancements facilitate stable performance under demanding catalytic conditions, thereby broadening their applicability in diverse fields, including adsorption and separation,[52] drug delivery,[53] bioimaging,[54] supercapacitors,[54] and catalysis.[55,56] Recently, ZIF-67 and its variants with adjustable shape and porosity have been produced using a range of synthetic techniques. These include sol–gel, solvothermal synthesis, surfactant-assisted methods, and microwave or ultrasound-assisted methods. In addition to producing high-quality ZIF-67, these techniques may successfully modify its porosity and crystal size by modifying variables like synthesis time and temperature.[56]

This review presents a thorough evaluation of ZIF-67 and its hybrid materials, with particular emphasis on their multifunctional roles in environmental remediation and energy-conversion technologies. Unlike previous reports that concentrate solely on adsorption or individual photocatalytic applications, this review uniquely combines both perspectives, demonstrating the potential of ZIF-67-based materials for clean-energy production (hydrogen and hydrogen peroxide generation) and environmental remediation *via* wastewater treatment and pollutant degradation. The dual-function approach highlights ZIF-67 as a highly adaptable material for green energy and environmental remediation and establishes a unified design principle for multifunctional photocatalytic systems targeting pressing global challenges. In order to address current limitations, this review systematically investigates the multifunctional performance of ZIF-67-derived materials in both energy production and environmental clean-up, highlights recent developments in their structural modification, including metal doping and semiconductor composite construction, and elucidates the key photocatalytic mechanism governing their performance. The synthetic strategies for ZIF-67 and its composite photocatalysts are comprehensively discussed, alongside a critical evaluation of their recent applications in energy conversion and environmental purification. Current challenges and future research directions are also outlined. Distinct from prior reviews that broadly address ZIF-67 synthesis or heterogeneous catalysis, this work focuses on ZIF-67-based hybrid frameworks and their photocatalytic mechanisms for integrated energy and environmental applications, providing a strategic foundation for the rational design of advanced ZIF-based photocatalysts (Fig. 3).[57]

2. Mechanism of formation

The synthesis of many metal–organic frameworks (MOFs) remains challenging due to the limited understanding of their formation mechanisms. This challenge is particularly pronounced for ZIF-67, where elucidating the formation process is essential for enabling scalable and commercially viable synthesis. Despite its significance, systematic studies aimed at deciphering the formation mechanism of ZIF-67 remain scarce. The formation of ZIF-67 has been hypothesized to be analogous to nanoparticle crystallization, as evidenced by its particle formation and diverse morphologies. However, the underlying formation mechanism has yet to be comprehensively elucidated.

ZIF-67 has attracted considerable attention for its enhanced performance in gas-separation applications. Extensive theoretical and density functional theory (DFT) studies have been conducted to elucidate its structural features, electronic properties, and gas-separation behaviour through computational

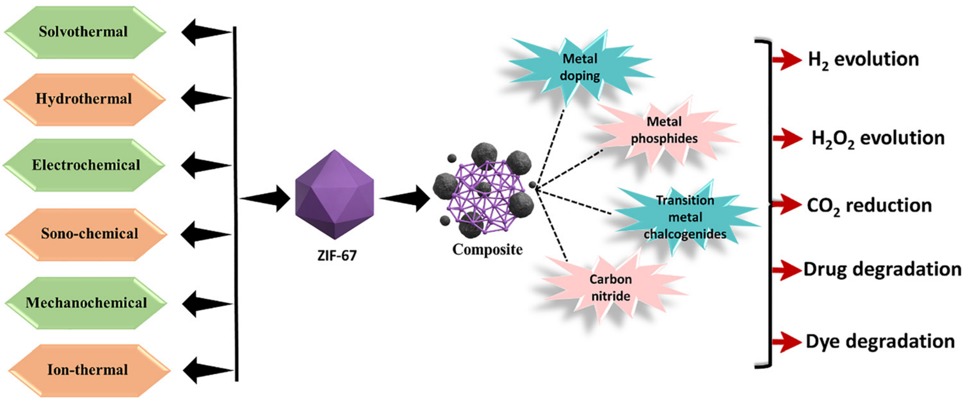

Fig. 3 Diagrammatic illustration summarizing the major themes and scope of this review.

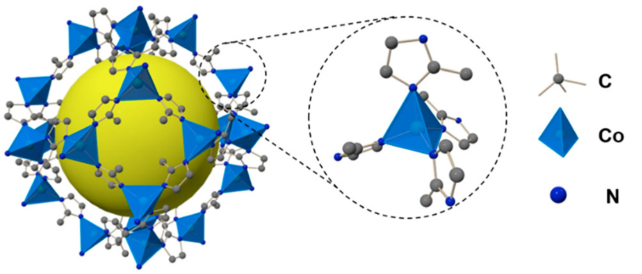

Fig. 4 3D representation of the ZIF-67 structure with void space depicted in a yellow coloured sphere; adapted with permission from ref. 58 © 2022 by the authors.

modelling. Structurally analogous to ZIF-8, ZIF-67 incorporates cobalt (Co) in place of zinc (Zn), a substitution that modifies its electronic structure and influences its overall structural stability.[58] The general structure of ZIF-67 is illustrated in Fig. 4. In ZIF-67, Co ions are tetrahedrally coordinated to four nitrogen atoms from imidazolate ligands, forming interconnected tetrahedral units.[59] The incorporation of Co centres results in a more compact framework compared to other ZIFs, particularly ZIF-8. Extensive theoretical investigations have been performed to elucidate the structural features of ZIF-67, including its bond angles and its response to applied pressure. In addition, molecular dynamics simulations have provided critical insights into the structural flexibility of the framework. Krokidas *et al.*[59] employed density functional theory (DFT) to calculate the electronic properties and optimize the molecular geometries of ZIF-67. Based on these DFT calculations, a force field specifically tailored for ZIF-67 was developed, incorporating detailed parameters for bond lengths, bond angles, torsional potentials, and nonbonded interactions. DFT calculations were further employed to determine the energy barriers associated with guest molecule diffusion, providing valuable insights into the separation performance of ZIF-67.

Experimental studies have correlated the kinetics of ZIF-67 with classical crystal growth models, with Feng *et al.* proposing a multistage process comprising nucleation, crystallization, growth, and steady state stages.[60] ZIF-67 formation commences with an incubation phase linked to the nucleation stage (I), where the relative crystallinity remains insignificant. Upon the completion of nucleation, the system transitions into the subsequent growth stage (II). The crystal growth kinetics of ZIF-67 follows the classical Avrami model, as described by the following equation:

$$y = 1 - \exp(-kt^{n}) \tag{1}$$

In this expression, y represents the relative crystallinity, k is the rate constant, t denotes the synthesis time, and n corresponds to the Avrami exponent. A decrease in pH was also observed, which is likely to promote the crystallization of the ZIF-67 framework by reducing the concentration of the deprotonated imidazole linker.[61] This stabilizes the neutral form of the linker and thereby limits further crystal growth. The relative crystallinity reaches a steady state (III), beyond which no appreciable variation is observed. Overall, the crystals progressively develop larger particle sizes and more pronounced faceting with time, as illustrated in Fig. 5a. Owing to the short synthesis duration of ZIF-67, it is hypothesized that crystallization is predominantly confined to the particle surface. Concurrently, the interior region may retain a medium-range ordered, metastable phase.[62] The medium-range order detected in ZIF-67 at early synthesis stages, marked by low relative crystallinity, is attributed to weak van der Waals intermolecular interactions that occur prior to the establishment of long-range crystalline order, eventually leading to a fully crystalline structure. The crystal planes are constructed from layers of Hmim ligands coordinated with Co ions, resulting in an irregular polygonal or rhombic dodecahedral morphology.[63] At this stage, crystal growth predominates and governs the ultimate morphology and size of the ZIF-67 crystals. In addition, the effect of the metal salt anions on the crystallization process was systematically investigated. *In situ* XRD characterization conducted by Feng and Carreon during their investigation of ZIF-67 crystallization kinetics revealed the presence of a low crystallinity, metastable intermediate phase during the synthesis process. Furthermore, SEM analysis tracking the evolution of

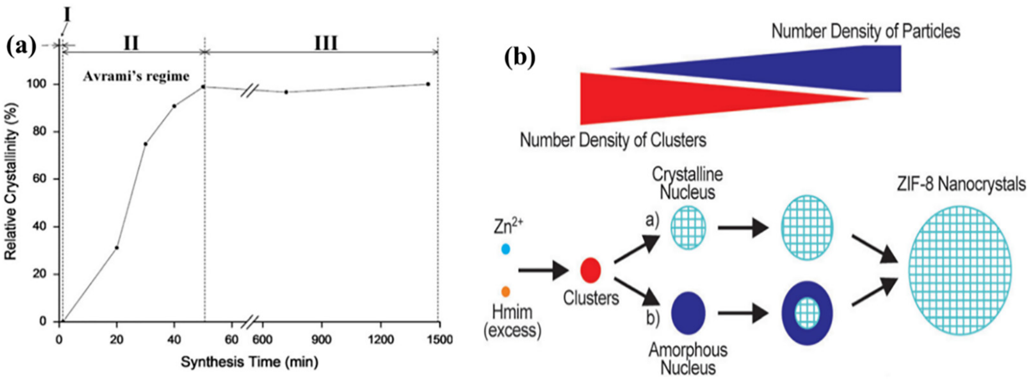

Fig. 5 (a) Variation of the relative crystallinity of ZIF-67 with synthesis time; adapted with permission from ref. 60 © 2015 Elsevier B.V. (b) Two alternative crystallization pathways showcasing the nucleation and growth of ZIF-67 nanoparticles; adapted with permission from ref. 62 © 2011 Wiley-VCH Verlag GmbH & Co. KGaA, Weinheim 8.

ZIF-67 particles demonstrated a time-dependent increase in the average particle size, consistent with an Ostwald ripening mechanism. The micrographs also revealed enhanced faceting, accompanied by the progressive sharpening of edges and corners of the ZIF-67 particles. In a separate study, the evolution of ZIF-67 particles was examined using FE-SEM imaging. An acid–base reaction, followed by the sequestration of leached metal ions, was employed to restructure the ZIF-67 crystals into diverse morphologies, including cubic, tetrahedral, and hollow box-like architectures. These etching studies demonstrated that crystals with higher surface functionality undergo more rapid etching and that the modulation of the etchant solution pH effectively controls the etching behaviour of ZIF-67 crystals. Moreover, the choice of metal precursors employed during synthesis plays a significant role in governing particle formation. Compared to NO_3^-, Cl^- possesses a smaller ionic radius and higher electron density, which leads to the formation of smaller ZIF-67 crystals when cobalt chloride hexahydrate ($CoCl_2.6H_2O$) is used as the precursor, relative to cobalt nitrate hexahydrate ($Co\ (NO_3)_2\cdot 6H_2O$). Moreover, more uniform and well-defined crystals were obtained when cobalt nitrate hexahydrate was employed, attributed to its higher salting-out effect and the relatively slower coordination kinetics between Co^{2+} and Hmim.

Based on an analogous study of the rapid nucleation and growth of ZIF-8 nanocrystals, a plausible formation mechanism for ZIF-67 can be proposed. Fig. 5b illustrates the nucleation and growth of ZIF-67 nanoparticles under conditions of high supersaturation. The nanocrystals are formed upon the interaction of Co^{2+} ions with an excess of Hmim ligands. Initially, small clusters are generated, which subsequently grow into ZIF-67 particles through successive monomer attachments until the clusters are fully consumed.[64] The formation mechanism of ZIF-67-based composites has also been systematically investigated. For example, Zhou *et al.* examined the key parameters governing the synthesis of NiCoFe-LDH@ZIF-67 for improved electrochemical performance. Their findings revealed that composite formation is primarily dictated by the hydrolytic acidity of the metal ions and their coordination affinity toward the organic ligands. The incorporation of foreign metal ions, such as Ni^{2+}, facilitated the formation of surface nanosheets and internal hollow architectures owing to their moderate hydrolytic acidity and strong coordination affinity toward nitrogen atoms. In contrast, the introduction of excessive Fe^{3+} disrupted the structural integrity, resulting in a flaky morphology rather than a hollow configuration. Additionally, the addition of metal ions led to a decrease in pH, thereby modulating hydrolysis behaviour, regulating the metal-ion valence states, and tuning the reaction kinetics, enabling precise control over the architecture of the composite ZIF-67.

3. Novelty of multimetallic ZIF-67 in energy and environmental applications

Thai *et al.*[65] developed a novel Mn/ZIF-67@GO bimetallic composite that exhibited remarkable efficiency in PMS activation for rapid ibuprofen removal. The Mn/ZIF-67@GO/PMS system achieved 98% removal of IBP (0.05 mM) within 15 min over a broad pH range (5–9), exhibiting excellent stability and minimal metal leaching ($<50\ \mu g\ L^{-1}$). The enhanced catalytic performance originates from the synergistic redox coupling between the Co and Mn centres embedded within the ZIF-67 framework and the conductive graphene oxide (GO) support, which improves electron transfer and the dispersion of active sites. Mechanistic investigations revealed that PMS activation proceeds through both radical ($SO_4^{\bullet-}$, OH, $O_2^{\bullet-}$) and nonradical ($^1O_2$) pathways, with singlet oxygen ($^1O_2$) identified as the dominant reactive species (Fig. 6a). Surface $\equiv$Co–OH and $\equiv$Mn–OH sites facilitate PMS adsorption and electron transfer, triggering cyclic Co(II)/Co(III) and Mn(II)/Mn(III)/Mn(IV) redox transformations, as confirmed by XPS analysis. Importantly, the intermetallic electron transfer between Co and Mn accelerates catalyst regeneration and sustains continuous ROS production. This dual radical–nonradical mechanism, combined with high stability and recyclability, highlights the novelty of multimetallic ZIF-67 systems as advanced platforms for sustainable antibiotic removal *via* sulphate-radical-based advanced oxidation processes.

Zhu *et al.*[66] reported the synergetic photocatalytic performance of bimetallic mixed ZIFs containing Co and Zn for enhanced degradation of organic pollutants under visible light irradiation. ZIF (1Zn:1Co) exhibited the highest photocatalytic activity, achieving up to 98.83% methylene-blue degradation under optimized conditions. The superior performance was attributed to the electronic synergy between Zn and Co within the crystal lattice, which enhanced charge separation and reactive-species generation. According to the principles of frontier molecular orbital theory, the photocatalytic process is controlled by the energy gap between the HOMO of the imidazole ligand and the LUMO of the metal nodes. Notably, the bimetallic ZIF displayed broader orbital distribution compared to its monometallic counterparts, facilitating greater electron capture and promoting radical formation *via* efficient electron transfer. DFT calculations further confirmed the enhanced orbital distribution and reduced recombination probability in ZIF (1Zn:1Co), explaining its superior catalytic performance. This study highlights how rational bimetallic engineering within MOF frameworks can tune electronic structure, improve visible light response, and significantly enhance photocatalytic efficiency (Fig. 6b–d).

Mengqing Hu *et al.*[67] developed a novel MOF-derived magnetic bimetallic catalyst, Ni/Co LDH@NC, synthesized through the carbonization of ZIF-67, followed by the solvothermal growth of Ni/Co-layered double hydroxide (LDH), for the simultaneous removal of sulfamethoxazole (SMX) and Pb(II) from wastewater *via* peroxymonosulfate (PMS) activation. The ZIF-67-derived nitrogen-doped carbon matrix provided a high surface area, enhanced conductivity, strong magnetism for easy recovery, and abundant oxygen vacancies (O_v), which served as active sites for PMS adsorption and activation. Under optimized conditions ($0.1\ g\ L^{-1}$ of the catalyst and $2\ g\ L^{-1}$ of the PMS), the catalyst achieved 100% degradation of SMX ($15\ mg\ L^{-1}$)

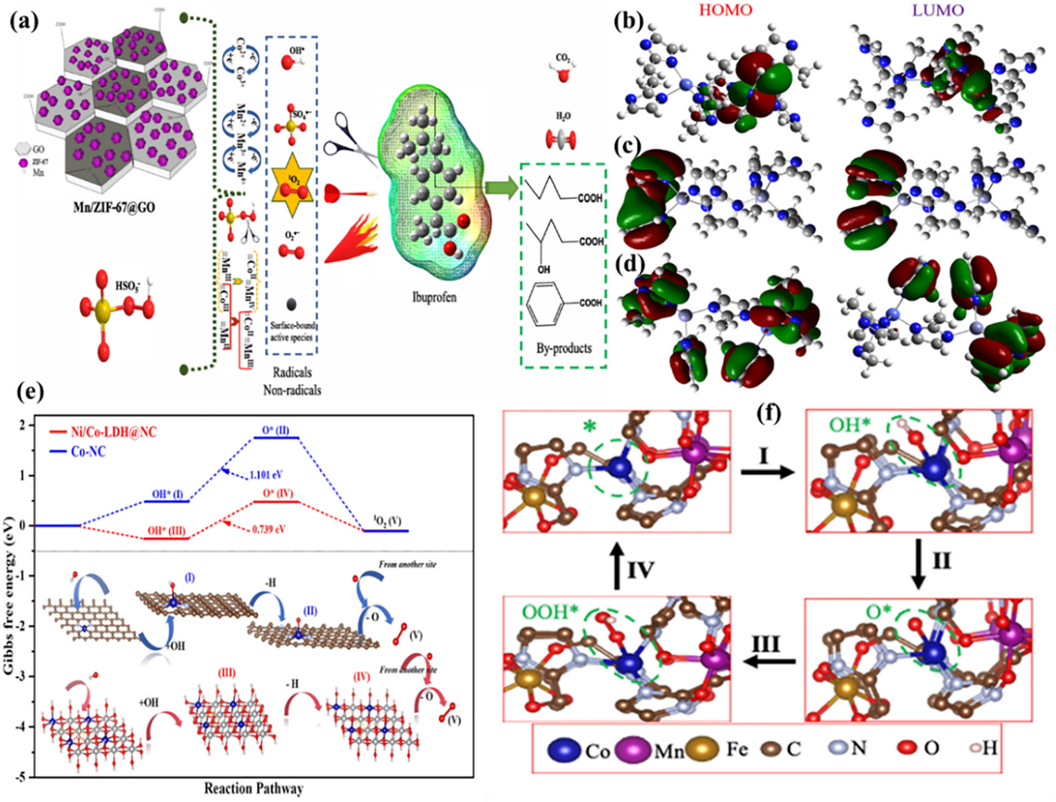

Fig. 6 (a) Mechanistic representation of PMS activation mediated by the Mn/ZIF-67@GO catalyst; adapted with permission from ref. 65 © 2023 Elsevier B.V. (b) HUMO and LUMO of ZIF-8, (c) ZIF-67, and (d) ZIF(1Zn:1Co). MO6//6-311 g** and ECP-LANL2TZ; adapted with permission from ref. 66 © 2022 Elsevier B.V. (e) Gibbs free energy comparison of Ni/Co LDH@NC and Co-NC catalysts at different catalytic sites following the proposed PMS activation pathway (PMS → OH* →O* → $^1O_2$); adapted with permission from ref. 67 © 2024 Elsevier B.V. (f) DFT investigation of the OER bimetallic and trimetallic ZIFs, highlighting the stepwise reaction pathway at the Co site with adsorbed intermediates (OH*, O* and OOH*) in the trimetallic structure; adapted with permission from ref. 68 © 2024 Elsevier Ltd.

within 20 min and a Pb(II) adsorption capacity of 90.3 mg g^{-1} within 2 h, while in mixed pollutant systems, it maintained complete SMX removal and 84% Pb(II) adsorption within 60 min, demonstrating strong anti-interference capability. Density functional theory (DFT) calculations revealed that PMS preferentially adsorbs onto Ni and Co bridging oxygen vacancy sites, undergoing O–O bond cleavage *via* the PMS → OH*→ O* → $^1O_2$ pathway, where SO_4* is released exothermically as H_2SO_4 and the rate-determining step is the OH* → O* conversion (Fig. 6e). Importantly, Ni/Co LDH@NC exhibited a lower Gibbs free energy barrier for this step compared to Co-NC, confirming that the synergistic interaction between adjacent Ni and Co sites enhances electron transfer, accelerates PMS decomposition, and promotes $^1O_2$ generation. Co primarily activates PMS while Ni modulates the electronic structure and facilitates interfacial charge transfer. The abundant bridging oxygen vacancies stabilize intermediates (OH* and O*) and reduce the overall reaction energy barrier. Toxicity analysis indicated that degradation intermediates were less harmful than SMX, and the catalyst maintained over 85% SMX degradation and 80% Pb(II) removal after four cycles, highlighting its stability and practical applicability. Overall, this work demonstrates that MOF-derived bimetallic heterostructures integrating electronic synergy, oxygen vacancy engineering, porous carbon conductivity, and magnetic separability offer an efficient and sustainable antibiotic and heavy metal remediation.

Zhwan Naghshbandi *et al.*[68] designed a trimetallic electrocatalyst, GO@ZIF-67@MnFe, by immobilizing Mn and Fe nanoparticles onto ZIF-67 grown on graphene oxide (GO) for enhanced oxygen evolution reaction (OER) performance for alkaline water splitting. Developed as a cost-effective alternative to noble metal catalysts, such as RuO_2 and IrO_2, the catalyst integrates the high surface area and tuneable porosity of ZIF-67; the excellent conductivity of GO; and the synergistic catalytic interactions among Co, Mn, and Fe. The optimized Mn : Fe (1 : 1) composition exhibited superior OER activity in 1.0 M KOH, achieving a low overpotential of 236 mV at 10 mA cm^{-2} and 380 mV at 100 mA cm^{-2}, a small Tafel slope of 55.7 mV dec^{-1}, an onset potential of 1.43 V, and excellent 24 h durability, outperforming ZIF-67, GO@ZIF-67, GO@ZIF-67@Mn, GO@ZIF-67@Fe, and other Mn/Fe ratios. The enhanced performance was attributed to the improved charge transfer and optimized adsorption of OER intermediates due to intermetallic synergy and conductive support effects (Fig. 6f). DFT calculations on ZIF-67, ZIF-67@Mn, ZIF-67@Fe, and ZIF-67@MnFe revealed that the formation of O* (OH* → O*) is the rate-determining step for all systems; however, ZIF-67@MnFe showed the lowest Gibbs free energy barrier (ΔG_2 = 2.25 eV) compared to ZIF-67@Mn (2.48 eV) and ZIF-67@Fe (2.33 eV), confirming the reduced activation energy in the trimetallic structure. Partial density of states (PDOS) analysis further demonstrated a strong overlap between the Co d-orbitals and the OH* p-orbitals in ZIF-67@MnFe, indicating enhanced electronic interaction and faster reaction kinetics. Overall, this study highlights a rational multi-metallic design strategy based on ZIF derivatives and graphene integration, emphasizing electronic synergy and structural engineering for developing efficient, durable, and low-cost OER electrocatalysts for sustainable hydrogen production.

4. A comprehensive overview of the ZIF-67 metal organic framework

Compared to Zn-based ZIFs, ZIF-67 exhibits superior redox activity and enhanced electrical properties owing to the intrinsically redox-active Co^{2+} centres. Efficient gas adsorption, separation, and catalytic reactions are made possible by its large surface area, strong microporosity (~10 Å pores), and remarkable durability in organic solvents and alkaline environments. For oxidation, hydrogenation, and other redox processes, the Co centres offer an abundance of active sites. Moreover, ZIF-67 effectively supports narrow bandgap semiconductors (such as TiO_2 and g-C_3N_4) by promoting charge transfer and reducing recombination, which improves photocatalytic H_2 evolution and pollutant degradation. These characteristics make ZIF-67 an adaptable platform for applications including energy conversion, storage, and environmental cleanup.

ZIF-67 is a material that is appealing for a variety of cutting-edge applications because, like ZIF-8, it demonstrates exceptional stability and resistance to degradation under challenging circumstances. Unlike most cobalt-based MOFs, ZIF-67 is uniquely insoluble in water, methanol, and common organic solvents, even under reflux conditions. The cobalt ions and imidazolate linkers form strong coordination bonds that mimic covalent bonding in solids, giving ZIF-67 its remarkable stability and robust structural integrity. Furthermore, the hydrophobicity of the ZIF-67 framework is essential for avoiding water-molecule intrusion, which might otherwise cause the metal–ligand coordination to become unstable. In aqueous or organic solvent environments, ZIF-67's porosity is optimized to promote selective adsorption and diffusion while thwarting hydrolysis, preserving its structure and functionality. Even under harsh chemical and thermal conditions, ZIF-67 is a useful material for catalytic, gas storage, and separation applications because of its high stability and flexibility (Fig. 7). The structural tunability of ZIF-67 enables the precise control of its characteristics, such as pore size, surface area, and metal coordination environment, by altering elements like the imidazolate linker, synthesis conditions, and metal selection (Co *vs.* other transition metals). These variables can be changed to adjust the electronic characteristics and catalytic behaviour of the ZIF-67 for particular uses. Notably, the catalytic properties of ZIF-67 are greatly enhanced by the cobalt centres, which permit redox reactions like catalytic degradation, hydrogenation, and oxidation. Furthermore, the metal centres promote the production of reactive oxygen species (ROS), such as superoxide anions and hydroxyl radicals, which are essential for photocatalytic reactions.

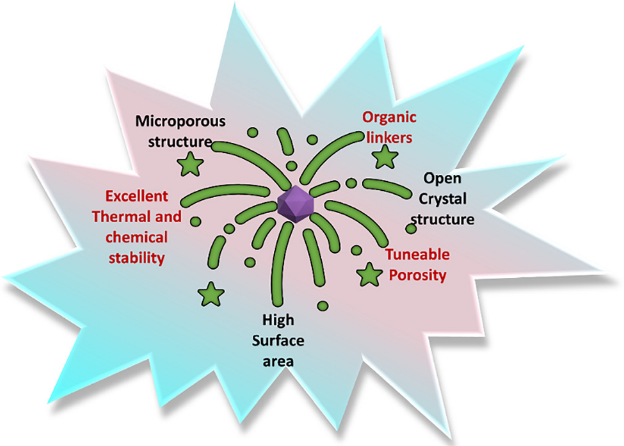

Fig. 7 Graphical overview of the key properties of ZIF-67.

Moreover, ZIF-67 has shown promise in photocatalytic applications, such as hydrogen generation and pollutant degradation. Combining ZIF-67 with narrow-bandgap semiconductors can improve the photocatalytic efficiency of composite materials by reducing electron–hole recombination and improving charge transfer. Additionally, it has been demonstrated that ZIF-67 stabilizes sensitive semiconductors, lowering photocorrosion and increasing the service life of photocatalytic systems. These characteristics provide long-term activity and stability in photocatalytic processes, making ZIF-67 an efficient protective layer for embedded semiconductors like Cu_2O. ZIF-67's design for certain applications, such as energy conversion, storage, and environmental cleanup, is also made possible by the flexibility of tailoring the metal centre and linker. The production of ZIF-67 necessitates meticulous control over variables, including temperature, solvent selection, agitation rate, and metal precursor concentration, similar to the case with ZIF-8. Several techniques, such as hydrothermal, electrochemical, and solvothermal methods, have been used to create ZIF-67 with specific characteristics for desired uses. It is possible to produce ZIF-67 with the necessary properties by manipulating these synthesis conditions, which makes it a strong and adaptable platform for a variety of chemical, environmental, and energy-related applications.

5. Methodological framework for synthesis

In recent years, a wide range of synthetic methodologies has been established for the fabrication of ZIF-67 and its derivatives with precisely tuneable morphologies and pore architectures, including solvothermal, surfactant-assisted, sol–gel, and microwave- or ultrasound-assisted routes. By adjusting the reaction parameters, precise tuning of the crystal size, morphology, and textural characteristics can be achieved. In order to create a homogenous gel network, the sol–gel process entails the slow hydrolysis and condensation of cobalt and organic precursors in a colloidal medium. The creation of ZIF-67-based composites or thin films with enhanced structural integrity and catalytic activity is made possible by this method, which guarantees the uniform distribution of active sites. Beyond enabling the synthesis of high-quality ZIF-67, these approaches allow the effective control of the crystal size and pore structure through the careful optimization of synthesis parameters, such as temperature and reaction time. The versatility of its synthetic strategies, coupled with the exceptional physicochemical properties of ZIF-67, renders it a highly attractive candidate for a wide range of applications, including volatile organic compound (VOC) adsorption, separation, supercapacitor production, and catalysis. Despite recent comprehensive reviews on ZIF synthesis and applications, their uses in heterogeneous catalysis have rarely been systematically addressed. Accordingly, a focused review on the synthesis and catalytic applications of ZIF-67-based materials is highly desirable.

5.1. Solvothermal synthesis

The most common method for making ZIF-67 is the solvothermal technique. In a typical process, 2-methylimidazole (Hmim) and cobalt sources are dissolved in solvents and heated in sealed autoclaves to temperatures between 50 °C and 200 °C. After 12 to 72 hours, well-defined crystals are produced. The three main steps of the formation process are typically hydrolysis, coordination, and deprotonation. By modifying the synthesis conditions, this sequence offers a practical way to modify and customize the properties of the materials.[69] For instance, Jayashree *et al.*[70] synthesized ZIF-67 using Co $(NO_3)_2{\cdot}6H_2O$ and 2-methylimidazole (Hmim) in two different organic solvents, methanol and dimethylformamide (DMF), under the same reaction conditions (60 °C for 4 h). Their methodical study showed that the solvent environment has a significant impact on the crystallization process and the resulting pore architecture. Significant morphological variations were evident in SEM micrographs, and distinct textural properties were confirmed by N_2 adsorption–desorption analyses.

Similarly, using methanol as the reaction medium at room temperature and allowing crystallization to continue for a full day, Qin *et al.* synthesized nanosized ZIF-67 crystals. The production of extremely homogeneous particles with superior monodispersity was made possible by this gentle and prolonged synthetic process. As shown in Fig. 8, a thorough morphological analysis verified that the products took on a distinct rhombic dodecahedral geometry. In addition to showing how crucial the reaction time and conditions are for nucleation and growth, this control over particle size and shape revealed the role of ambient temperature in the synthesis of architecturally precise ZIF-67 nanocrystals.[71] However, it is impossible to ignore the problems of excessive energy use and environmental contamination that come with traditional synthesis methods, especially given the widespread use of hazardous solvents.[72,73] The establishment of green synthesis routes has shifted the focus of ZIF preparation toward environmental sustainability and energy conservation, such as through the use of water as the reaction medium.[74] Since the aqueous synthesis of ZIF-8 at room temperature was demonstrated,[39] water has progressively taken the place of organic solvents in the production of ZIF-67.[75] Critical factors, such as the reactant concentration, synthesis duration, and pH, have been carefully studied to regulate the structural and morphological features of ZIF-67.

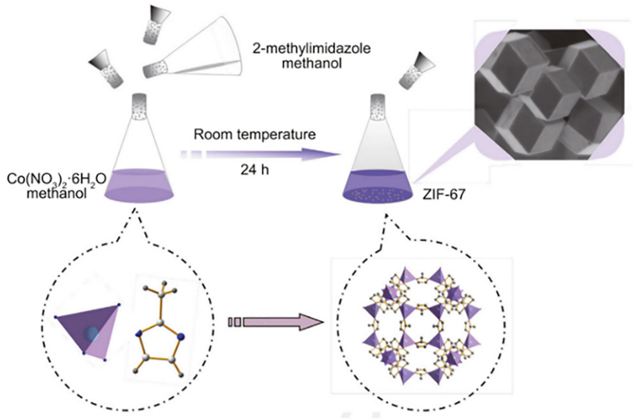

Fig. 8 Depiction of the proposed synthetic pathway for ZIF-67; adapted with permission from ref. 76 © the Royal Society of Chemistry 2015.

Zhang *et al.*[76] reported that combining Co $(NO_3)_2$ and Hmim in water produces a zeolitic imidazolate salt framework (ZIF-L-Co), identified as an intermediate phase during ZIF-67 formation. By altering the molar ratios or precursor concentrations, the phase and morphology of the materials were successfully managed. Increasing the Hmim/Co^{2+} molar ratio from 8 to 24 caused a morphological change from leaf-like sheets to rod-like structures, as shown in Fig. 9. The rough polyhedral became smoother with noticeable corners and edges when the ratio was increased to 32–48. Under vacuum heating or water-vapor-assisted conditions, ZIF-67 crystallized *via* a solid transformation mechanism. Importantly, the phase transition from ZIF-L-Co to ZIF-67 was accelerated by water. Further, higher precursor concentrations combined with lower Hmim/Co^{2+} ratios promoted ZIF-L-Co crystallization.

Civan *et al.*[77] subsequently developed an aqueous synthesis process for ZIF-67 from $Co(OAc)_2{\cdot}4H_2O$ and Hmim, where precise pH-controlled etching yielded a range of morphologies, including truncated rhombic dodecahedra, cubes, tetrahedra, and hollow box structures, without loss of porosity. Parts of the original cobalt ligand 2D framework were successfully broken down by the etching solvent by sequentially protonating ligands, breaking coordination bonds, and releasing Co^{2+} ions.

5.2. Surfactant-assisted method

The surfactant-assisted method involves the addition of surfactants to the precursor solution to improve dissolution

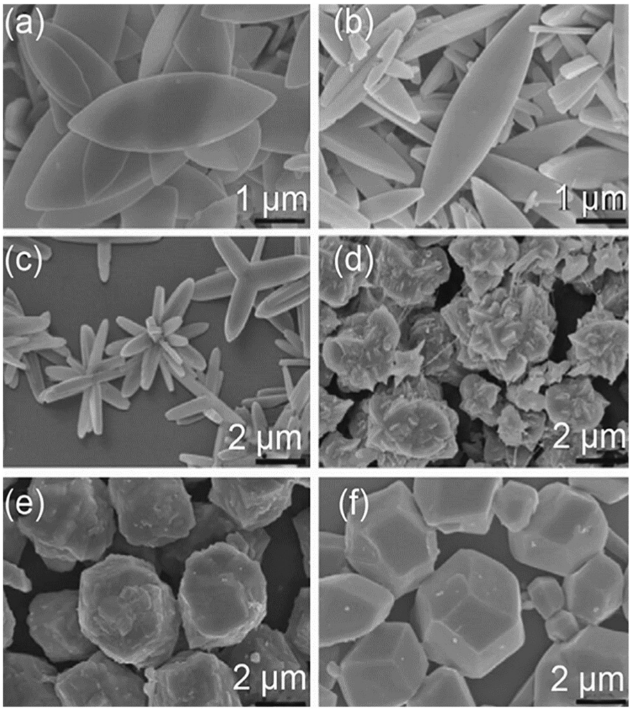

Fig. 9 SEM pictures of samples obtained with various Hmim/Co molar ratios of (a) 8, (b) 16, (c) 24, (d) 32, (e) 40, and (f) 48; adapted with permission from ref. 76 © the Royal Society of Chemistry 2015.

behaviour and promote controlled growth, resulting in uniformly dispersed product particles. Furthermore, by altering the kind and concentration of surfactants, the morphology and structural characteristics of the samples can be precisely customized.[78] For example, ZIF-67 can be synthesized quickly (∼5 min) by combining an aqueous Hmim solution containing cetyltrimethylammonium bromide (CTAB) with a cobalt precursor. As a capping agent in this process, CTAB makes it possible to precisely control the particle size during crystal growth within the 50–320 nm range. Li *et al.* recently reported synthesizing Fe_2O_3@ZIF-67 composites by immersing Fe_2O_3 nanorods in DMF containing polyvinylpyrrolidone (PVP), adding Hmim and $Co(NO_3)_2{\cdot}6H_2O$, and then drying for 12 hours at 80 °C (Fig. 10a). PVP performed two roles in this strategy: (i) it operated as a caping agent to regulate the size of the product, and (ii) it coordinated Co^{2+} ions with the pyrrolidone (C═O) groups to act as a molecular linker and improve the connection between ZIF-67 and Fe_2O_3 nanorods.

In the ZIF synthesis, surfactants function as soft structure-modifying agents that facilitate the formation of mesopores and hierarchical architectures without altering the intrinsic crystal structure of the framework. Duan *et al.* achieved the rapid fabrication of hierarchically porous ZIF-67 at room temperature and atmospheric pressure by utilizing three surfactants, namely tetrabutylammonium hydroxide (TBAOH), tetrapropylammonium hydroxide (TPAOH), and tetraethylammonium hydroxide (TEAOH). The development process of hierarchical ZIF-67 was elucidated by both modelling and experimental research, as shown in Fig. 10b. The surfactants were bifunctional modulators in this process, acting as both structure-directing agents (SDAs) and deprotonation agents at the same time. These surfactants regulated the development of mesoporous and microporous channels during crystal growth, enhanced the coordination between Hmim and Co^{2+}, and facilitated rapid deprotonation. After the activation and drying procedures, the hierarchical structure was produced. The incorporation of *N*,*N*-dimethyl-1,2-ethanediamine enabled the rational engineering of hierarchical pore architecture in microporous ZIF-67, thus broadening its structural versatility.[79]

5.3. Sol–gel method

Sol–gel methodology has evolved into an effective and flexible technique that facilitates the design of hierarchical frameworks with tuneable molecular compositions. This method connects molecular-level chemistry with macroscopic material properties by modifying chemical pathways during hydrolysis and condensation to create materials with adjustable morphology, porosity, and functionality. Usually, MOF precursors undergo hydrolysis and condensation in conjunction with coagulants to produce a colloidal suspension of submicrometer particles. After that, heat treatment turns gels with distinct spatial structures into solid particles. For example, Yang *et al.*[80] reported a sol–gel method for synthesizing a three-dimensional rGO/ZIF-67 (reduced graphene oxide aerogel). As shown in Fig. 11a, the process critically relies on the staged addition of ZIF precursor solutions to the pre-formed three-dimensional rGO structure, avoiding a one-step mixing approach. Cobalt ions were anchored onto the rGO surface and then coordinated with Hmim due to the high adsorption

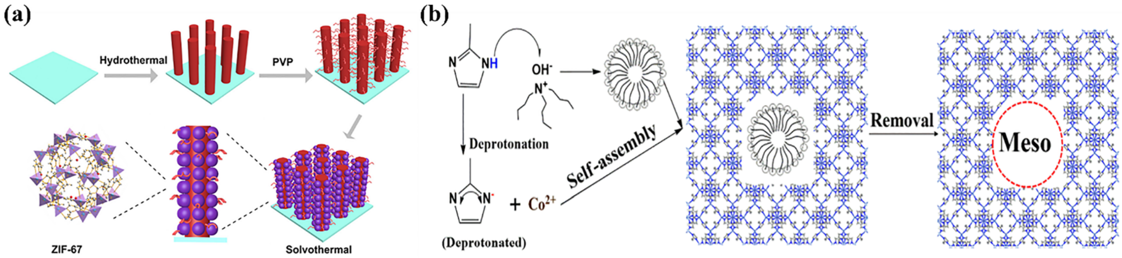

Fig. 10 (a) Schematic of the preparation route for the Fe_2O_3@ZIF-67 composite; adapted with permission from ref. 78 © 2019 Elsevier B.V. (b) Mechanism of hierarchically porous ZIF-67 formation; adapted with permission from ref. 79 © 2018 the American Chemical Society.

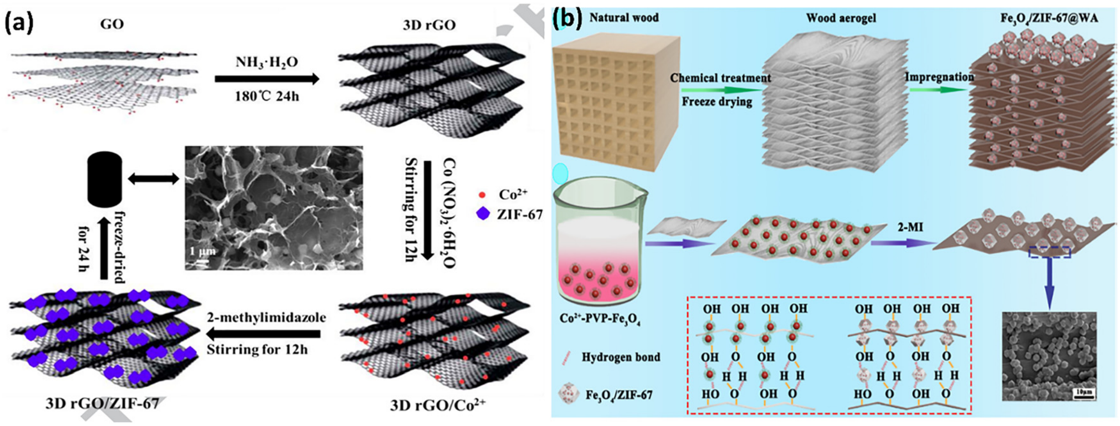

Fig. 11 (a) Diagram for the synthesis of 3D rGO/ZIF-67; adapted with permission from ref. 80 © 2018 Elsevier B.V. (b) Diagrammatic representation of the Fe_3O_4/ZIF-67@WA aerogel preparation procedure; adapted with permission from ref. 81 © 2019 Elsevier Ltd.

affinity of rGO for metal ions. The 3D rGO/ZIF-67 hydrogel was converted into an aerogel by freeze-drying.

Xu *et al.*[81] *in situ* integrated magnetic Fe_3O_4/ZIF-67 within a lightweight natural wood aerogel (WA) matrix to construct a hierarchically porous Fe_3O_4/ZIF-67@WA composite. To enable the anchoring of Co^{2+}-decorated Fe_3O_4 NPs onto the wood aerogel framework, Fe_3O_4 nanoparticles (NPs) were first treated with a Co^{2+} solution containing polyvinylpyrrolidone (PVP), as shown in Fig. 11b. While the presence of Hmim encouraged the nucleation and growth of ZIF-67 crystals on the WA surface, the plentiful oxygen-containing functional groups in the cellulose chains enabled strong hydrogen bonding and electrostatic interactions. It is noteworthy that instead of penetrating the internal porous network of WA, Fe_3O_4 and ZIF-67 NPs were primarily immobilized on the aerogel surface.

5.4. Microwave/ultrasound-assisted method

In recent years, there has been an increasing interest in the synthesis of ZIF-67 with the aid of ultrasound or microwave technology. By producing transient high-temperature and high-pressure microenvironments, these methods improve structural purity, produce particles with a uniform size distribution, speed up crystallization, and significantly reduce reaction time. A simple ultrasound-assisted method for creating a ZIF-67@Fe_3O_4@ESM (eggshell membrane) composite was presented by Niyaz *et al.*[82] (Fig. 12). This method involved first sonicating a cobalt nitrate solution, combining it with presynthesized Fe_3O_4@ESM in the aqueous phase, and finally sonicating it again with Hmim present. ZIF-67 crystals were successfully grown along the highly interwoven, crosslinked protein fibres of the ESM, according to SEM analysis. By increasing the local turbulence and liquid microcirculation, the ultrasound-assisted procedure accelerates the coordination dynamics and cuts the reaction time from 6 hours (with traditional stirring) to just 3 hours.

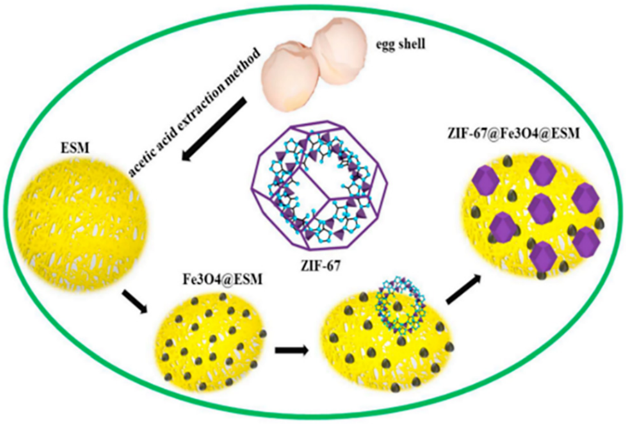

Fig. 12 Schematic representation of the ZIF-67@Fe_3O_4@ESM synthesis process; adapted with permission from ref. 82 © 2019 Elsevier B.V.

Tu *et al.*[83] also reported fabricating ZIF-67 with a specially designed microwave-assisted synthesis system that included a cooling module, time control unit, microwave generator, and sample chamber. ZIF-67 was made using a solvent that contained a mixture of ethanol and methanol. In contrast to traditional heating, microwave irradiation does not rely on surface conduction but rather uses the precursor solution itself as the heat source. Thus, the instantaneous generation of high temperatures greatly reduces the total synthesis time and speeds up growth kinetics. Additionally, it provided improved control over the shape and size of nanoparticles. In a pioneering study, Febrian *et al.*[84] employed a one-step microwave-assisted strategy to fabricate a CoZn-ZIF-8 membrane using 2-methylimidazole (Hmim) as the ligand and mixed metal ions (Zn^{2+} and Co^{2+}). Under microwave radiation at about 100 W, the entire process was finished in about 1.5 min. There is significant potential for the scalable and industrial production of ZIF-67 materials with such a quick and eco-friendly approach. The microwave-assisted method is a viable environmentally friendly strategy for the industrial production of ZIF-67. However, sustaining accelerated crystallization requires specialized instrumentation and additional energy input, which can significantly increase energy consumption and ultimately raise production costs and operating complexity.[85]

5.5. Other methods

In conjunction with the methods mentioned above, new specialized approaches for ZIF-67 preparation have emerged recently. For instance, Cristina *et al.*[86] used CoO and Hmim powders to create microporous ZIF-67 using a novel and straightforward technique called accelerated aging that eliminates the need for high temperatures, bulk solvents, and constant agitation. Even though ZIF-67 has a high thermal stability, its microporous structure can form under mild, diffusion-controlled conditions through the self-assembly of ligands with cobalt oxide. Proton-donating salts like $(NH_4)_2SO_4$ activate Hmim through acid catalysis, which strengthens its coordination with CoO and drives the formation of ZIF-67. Furthermore, the system's reaction to relative humidity was investigated. The findings showed that, even though the sample stayed in powder form, a small increase in relative humidity significantly increased yield and accelerated the reaction.

To enable the integration of ultra-low-k MOF dielectrics into chip interconnects, Krishtab *et al.*[87] investigated the conversion of cobalt oxides into ZIF-67 using a chemical vapor deposition (CVD) approach. Two synthetic routes served as the basis for this procedure, as shown in Fig. 13. Route A involved filling the trenches by applying a conformal oxide/hydroxide coating to the metal lines. Route B, however, used selective controlled oxidation, which proved superior as the CoOx precursor formed a uniform layer and eliminated leakage issues between capacitor forks. Upon exposure to Hmim vapor, the metal oxide precursor was progressively consumed, triggering nucleation and its subsequent conversion into a porous MOF-CVD ZIF thin film. This technique made it possible to deposit a ZIF-67 film with constant thickness in a controlled and consistent manner.[88] This technique is essential for integrating MOFs into chip interconnects and establishing a rational link between the production of microelectronics and state-of-the-art MOF materials. Du *et al.*[89] also suggested electrochemical deposition as an additional technique for producing porous, high-throughput ZIF-67. Instead of employing Co^{2+} salts, the mechanism is primarily controlled by the constant anodic dissolution of the Co metal, which supplies Co(II) ions to the reaction medium consisting of Hmim in ethanol and hexadecyltrimethylammonium bromide as the electrolyte in a two-electrode cell. A redox reaction on electrodes triggered by ion migration produced the ZIF-67 coating, and the applied voltage was all that was needed to regulate the reaction rate. This method eliminates the interference caused by anions, such as No_3^- and Cl^-, allowing for continuous, high throughput, and inexpensive synthesis at atmospheric pressure and room temperature.

The reverse microemulsion technique enables precise control over the size and morphology of monodisperse crystals. Using a water-in-oil system composed of CTAB, 1-hexanol, and heptane, Sun *et al.*[90] successfully synthesized ZIF-67 at room temperature. The product showed significantly higher surface area and pore volume than aqueously synthesized ZIF-67, as well as uniform particles and good thermal stability. The presence of multiple nano-reactors or micelles, which act as confined environments that promote the reaction between metal ions and ligands, controls the process. By guaranteeing that the reaction is spatially constrained within the nano-reactors, this confinement enables exact control over the crystal size. The dynamic light scattering (DLS) measurements employed in this work are important because they quantify the dimension of the micelle, which is important for estimating the eventual size of the crystalline products.

6. Emerging applications of ZIF-67-based materials

6.1. Energy conversion

Energy conversion involves redox-driven processes that transform light, electrical, or chemical energy into sustainable fuels and value-added products. In reactions such as hydrogen evolution, oxygen reduction, and CO_2 reduction, photon or

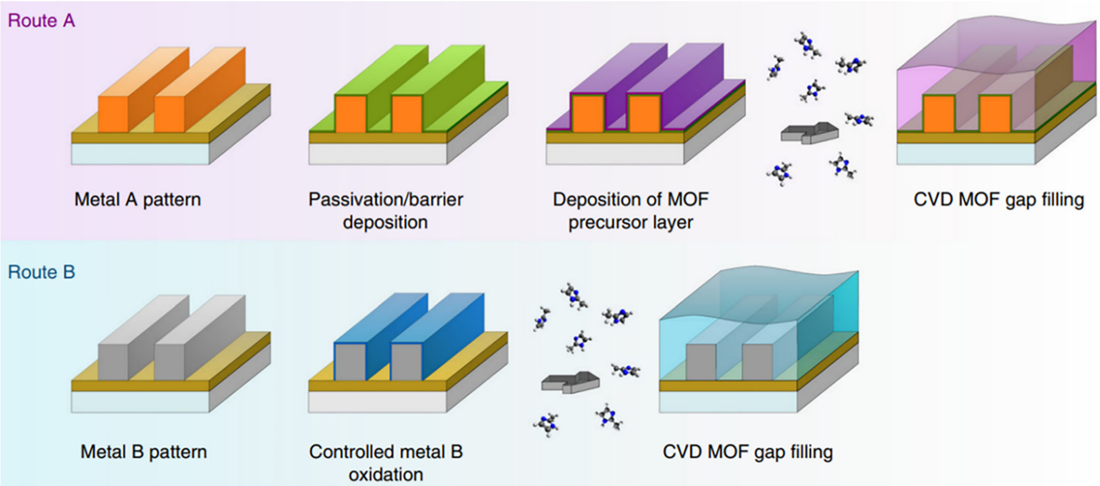

Fig. 13 Schematic of two synthetic strategies for ZIF-67 *via* CVD; adapted with permission from ref. 87 © 2019 the author(s).

electron input generates charge carriers that drive selective oxidation and reduction. Artificial photosynthesis integrates light harvesting with CO_2 fixation or water splitting to produce solar fuels, while electrocatalysis stores renewable energy in the chemical bonds of H_2, hydrocarbons, or H_2O_2. These approaches support energy storage, reduce greenhouse gas emissions, and promote carbon-neutral cycles.

6.1.1. H_2 evolution. One of the most promising strategies for addressing the global energy crisis is the evolution of photocatalytic hydrogen from water splitting. This method provides a practical way to decrease dependency on fossil fuels and reach carbon neutrality by directly transforming the abundant solar energy into sustainable and clean hydrogen fuel.[91] Three interconnected steps control the entire photocatalytic water-splitting process: (1) electrons from the valence band (VB) are excited from the valence band to the conduction band (CB) by incident light with energy greater than the bandgap; (2) the photogenerated charge carriers are separated and carried to the surface active sites; and (3) reduction and oxidation half-reactions take place, in which VB holes oxidize water molecules to produce O_2 and CB electrons convert H^+ ions into H_2. The crucial redox pathways controlling photocatalytic hydrogen production are represented by these processes.[92]

$$\text{Oxidation} - 2H_2O \rightarrow O_2 + 4H^+ + 4e^- \quad E_0 = 1.23\ \text{eV} \qquad (2)$$

$$\text{Reduction} - 2H^+ + 2e^- \rightarrow H_2 \quad E_0 = 0.00\ \text{eV} \qquad (3)$$

$$\text{Overall} - 2H_2O \rightarrow O_2 + 2H_2 \quad E_0 = 1.23\ \text{eV} \qquad (4)$$

For water splitting, the valence band (VB) must lie above +1.23 V *vs.* NHE to drive O_2 evolution, while the conduction band (CB) must fall below 0 V *vs.* NHE to promote H^+ reduction to H_2. These band edge locations determine the viability of total water splitting, as shown in Fig. 14a.[44]

According to Li *et al.*,[93] Co-based ZIF-67 achieves efficient H_2 evolution due to the favourable hydrogen adsorption of Co^{2+} and its partially filled 3d orbitals that enhance charge transport. Heteroatom modifications (S, O, P) adjust the electronic structure, forming asymmetric Co active sites that promote proton adsorption and hydrogen reduction. S doping induces charge polarization, O-modification introduces Co^{2+}/Co^{3+} states, and phosphodation creates strong Co-P coordination with effective orbital hybridization, enabling dual-site catalysis and improved HER kinetics with a lower Tafel slope (153–88 mV dec^{-1}), consistent with the Volmer–Heyrovsky mechanism (Fig. 14b). DFT results confirm the strong H and H_2O adsorption on the Co-P sites, supporting the dual protonation pathway and efficient charge transfer under visible light (Fig. 14c). In the presence of Eosin Y and TEOA, rapid electron transfer to Co-P centres lowers the reaction barrier. While S- and O-modified ZIF-67 show slight enhancements in H_2 evolution (7 and 13 μmol, respectively) and pristine ZIF-67 exhibits minimal yield (4 μmol), phosphorated ZIF-67 shows a remarkable increase to 317 μmol without altering the morphology, as evidenced by SEM (Fig. 14d).

Khan *et al.*[94] reported that coupling ZIF-67 with g-C_3N_4 markedly improves catalytic activity. Pristine ZIF-67 suffers from poor conductivity and rapid charge recombination, but forming a heterojunction with nitrogen-rich g-C_3N_4 enhances the Co–N_x stability, promotes directional charge transfer, and suppresses recombination. The π-conjugated 2D g-C_3N_4 sheets also improve electrolyte contact and bubble release, create a mesoporous structure with higher surface area, and lower charge-transfer resistance. Unlike rGO or CNTs, g-C_3N_4 acts as both a conductive mediator and a cocatalyst. The optimized 3 wt% g-C_3N_4@ZIF-67 shows low overpotentials (176 mV for the HER and 152 mV for the OER at 10 mA cm^{-2}). Characterization confirms the preserved crystallinity, high surface area, reduced resistance, and strong hydrophilicity (54.40°), supporting its efficient performance (Fig. 14e).

You *et al.*[95] fabricated a hollow CdS@Mn-ZIF-67 heterostructure as a visible light dual photocatalyst for H_2 evolution and tetracycline degradation. A SiO_2-templated method produced hollow CdS spheres coated with Mn-ZIF-67, yielding a mesoporous (∼5.5 nm), high surface area (131.1 $m^2\ g^{-1}$) composite (Fig. 14f). The Mn-ZIF-67 shell suppresses CdS recombination and photocorrosion, while the type-II heterojunction promotes electron transfer to CdS for H_2 evolution and hole migration to Mn-ZIF-67 for effective charge separation. The optimized CdS@Mn-ZIF-67 achieved 94.8% tetracycline degradation in 60 min and a high H_2 evolution rate of 10 889.2 μmol $h^{-1}g^{-1}$, 74 times higher than that for Mn-ZIF-67 and 5 times higher than that for hollow CdS (Fig. 14g).

Gong *et al.*[96] prepared a $Zn_{0.5}Cd_{0.5}S$/ZIF-67 hybrid *via in situ* growth, where dodecahedral ZIF-67 anchored well-dispersed ZnCdS nanoparticles to form a cooperative heterojunction. While ZIF-67 offers high porosity but low activity and ZnCdS suffers from photocorrosion and recombination, their integration enables efficient charge mediation and structural stabilization. Band gaps of 2.34 eV (ZnCdS) and 1.67 eV (ZIF-67) with matched CB levels enable directional electron transfer from ZIF-67 to ZnCdS and hole migration in the reverse direction, suppressing photocorrosion. DFT verified the strong H adsorption on the ZCS (111) surface (1.6587 eV) (Fig. 14h–i). The optimized composite (ZZ3) achieved 23 246 μmol $h^{-1}g^{-1}$ H_2 evolution, far exceeding the results achieved with ZCS and ZIF-67 (Fig. 14j), due to effective interfacial charge separation. It retained 82.7% activity after 20 h (Fig. 14k) and showed a maximum AQE of 6.95% at 420 nm (Fig. 14l), confirming its efficient visible light–driven performance and stability.

In summary, pristine ZIF-67 exhibits limited photocatalytic H_2 evolution due to its poor conductivity and rapid charge recombination; however, its activity can be significantly enhanced through heteroatom doping, phosphidation, and heterojunction engineering. The formation of Co–P dual active sites optimizes the electronic structure and accelerates proton reduction kinetics. Simultaneously, integration with semiconductors, including g-C_3N_4, CdS, and $ZN_{0.5}Cd_{0.5}S$, promotes efficient interfacial charge separation *via* type-II band alignment. These combined effects demonstrate that electronic-structure tuning and rational heterojunction design are central

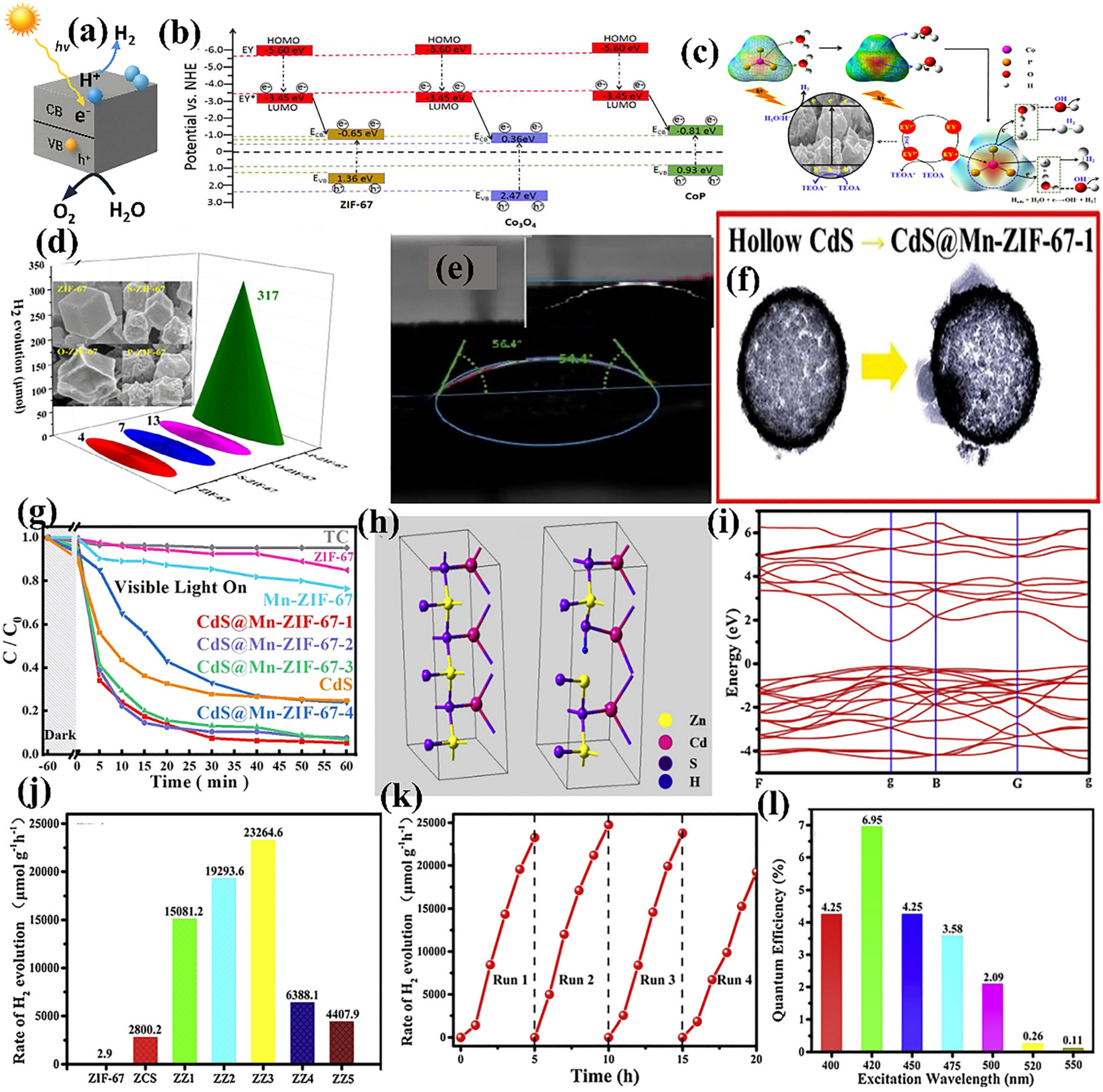

Fig. 14 (a) Photocatalytic hydrogen generation through water splitting; (b) comparison of the HOMO and LUMO of eosin Y and the conduction band and valence band of the ZIF-67-derived samples; optimized CoP (111) surface; adapted with permission from ref. 93 © 2019 Elsevier B.V. (c) Mechanism analysis of hydrogen evolution; adapted with permission from ref. 93 © 2019 Elsevier B.V. (d) H_2 evolution activities of ZIF-67, S-ZIF-67, O-ZIF-67 and P-ZIF-67; adapted with permission from ref. 93 © 2019 Elsevier B.V. (e) Contact angle of g-C_3N_4/ZIF-67; adapted with permission from ref. 94 © 2023 the author(s). (f) STEM-HAADF of the hollow composite photocatalyst (CdS@Mn-ZIF-67-1); adapted with permission from ref. 95 © the Royal Society of Chemistry 2020. (g) Photocatalytic activity results of all samples; adapted with permission from ref. 95 © the Royal Society of Chemistry 2020. (h) Calculation model for the pure samples of ZCS; adapted with permission from ref. 96 © 2020 Elsevier B.V. (i) Band structure of ZCS; adapted with permission from ref. 96 © 2020 Elsevier B.V. (j) Hydrogen-evolution rate diagram of the pure ZCS, ZIF-67, and ZZx (x, different contents of ZIF 67); adapted with permission from ref. 96 © 2020 Elsevier B.V. (k) Hydrogen production stability test of ZZ3; adapted with permission from ref. 96 © 2020 Elsevier B.V. (l) Apparent quantum efficiency of ZZ3 in the 400–550 nm wavelength range; adapted with permission from ref. 96 © 2020 Elsevier B.V.

to enhancing the hydrogen evolution performance of ZIF-67-derived catalysts, reinforcing their promise for solar water-splitting applications (Table 1).

6.1.2. H_2O_2 generation. Hydrogen peroxide (H_2O_2) is a multipurpose, eco-friendly oxidant and reductant that is widely used in industrial chemistry and has shown great promise as a high-energy fuel option for next-generation fuel cells.[100] H_2O_2 can be produced by a more straightforward one-step two-electron reduction process or by a two-step single-electron reduction pathway. Whereas the electrons in the conduction band (CB) help reduce the adsorbed O_2 to H_2O_2, the photogenerated holes in the valence band (VB) oxidize H_2O to O_2 and H^+ in photocatalytic systems. From the standpoint of photoelectrochemistry, the one-step two-electron reduction pathway

Table 1 Overview of various ZIF-67-derived MOF nanocomposites and their efficiencies in photocatalytic hydrogen evolution

S. no.	Materials	Methods	Activity (μmol)	Tafel slope (mV dec^{-1})	Quantum yield (%)	Ref.
1	$g\text{-}C_3N_4$@ZIF-67/(10%wt) NiS_x	Solvothermal	573	165	12.2	97
2	$Zn_{0.5}Cd_{0.5}S$/ZIF-67	Solvothermal	23 264.6	—	6.95	96
3	ZIF-67@CoFe LDH	Solvothermal	350	—	—	98
4	CoP@C/CdS	Hydrothermal	264.6	—	—	99

is thought to be the more effective way to produce H_2O_2.[101,102] The sequential reactions described in eqn (5)–(9) follow the two-step single-electron pathway. Eqn (10), on the other hand, shows the one-step two-electron pathway, which directly couples O_2 with two H^+ to produce H_2O_2. Eqn (11) provides the following summary of the entire photocatalytic reaction.

$$2H_2O + 4h^+ \rightarrow O_2 + 4H^+ \quad (5)$$

$$O_2 + e^- \rightarrow O_2^{\bullet-} \quad (6)$$

$$O_2^{\bullet-} + H^+ \rightarrow HO_2^{\bullet} \quad (7)$$

$$HO_2^{\bullet} + e^- \rightarrow HO_2^- \quad (8)$$

$$HO_2^- + H^+ \rightarrow H_2O_2 \quad (9)$$

$$O_2^- + 2H^+ + 2e^- \rightarrow H_2O_2 \quad (10)$$

$$2H_2O + O_2 \rightarrow 2H_2O_2 \quad \Delta G_0 = 117\ \text{kJ mol}^{-1} \quad (11)$$

The photocatalytic conversion of H_2O and O_2 into H_2O_2 is thermodynamically disfavoured, exhibiting a standard Gibbs free energy change (ΔG°) of 117 kJ mol^{-1}.

Ji *et al.*[103] demonstrated that integrating $g\text{-}C_3N_4$ with a ZIF-67-derived CoP/Co cocatalyst encapsulated in N,P-doped carbon (Cop/Co@NPC) significantly enhances photocatalytic H_2 and H_2O_2 production (Fig. 15a). The synergistic effect of CoP, metallic Co, and conductive heteroatom-doped carbon improves charge separation and selectively promotes the two-electron pathway, *i.e.*, $O_2^{\bullet-} \rightarrow H_2O_2$. CoP provides efficient electron extraction and $O_2^{\bullet-}$ activation sites, while metallic Co acts as an electron relay, suppressing recombination in $g\text{-}C_3N_4$. The uniformly dispersed Co/CoP domains (0.20 nm for Co (111) and 0.19 nm for CoP (211)) are embedded in a conductive N, P-doped carbon matrix that stabilizes H_2O_2 and prevents its back decomposition. When coupled with exfoliated $g\text{-}C_3N_4$, an electron cascade system is formed (Fig. 15b), enabling rapid electron transfer and selective two-electron ORR, as confirmed by time-resolved H_2O_2 evolution measurements (Fig. 15c). Overall, the CoP/Co@$g\text{-}C_3N_4$ heterostructure integrates efficient light harvesting, fast interfacial transport, and regulated H_2O_2 adsorption (Fig. 15d), serving as a model system for selective and efficient H_2O_2 generation.

Chen *et al.*[104] developed a ZIF-67-derived Co_3O_4@CN/$g\text{-}C_3N_4$ heterojunction that significantly enhances visible light H_2O_2 production. Uniformly anchored Co_3O_4@CN improves charge separation, oxygen adsorption, surface area, and light harvesting. The optimized ZCN-10 achieved 531.1 μM H_2O_2 evolution (2655.3 μmol g^{-1} h^{-1}) in 1 h, about 3.5 times higher than that achieved with pristine $g\text{-}C_3N_4$, with excellent stability over five cycles. Strong DMPO $O_2^{\bullet-}$ signals in the EPR spectra (Fig. 15e) under illumination confirm $O_2^{\bullet-}$ as the key intermediate in the two-step ORR pathway, while no signal appears in the dark. Kinetics studies (Fig. 15f) show a higher rate constant for ZCN-10 (8.7 μM min^{-1}) than $g\text{-}C_3N_4$ (2.6 μM min^{-1}), indicating faster electron transfer. The proposed mechanism (Fig. 15g) shows electrons transferring from $g\text{-}C_3N_4$ to Co_3O_4@CN to reduce O_2 to H_2O_2, while ethanol scavenges holes, leading to efficient charge separation and selective H_2O_2 generation.

In summary, photocatalytic H_2O_2 generation using ZIF-67-derived systems is markedly improved through heterostructure engineering that promotes selective two-electron oxygen reduction and efficient charge separation. Architectures such as CoP/Co@NPC/$g\text{-}C_3N_4$ and Co_3O_4@CN/$g\text{-}C_3N_4$ enhance O_2 activation, accelerate interfacial electron transfer, and suppress the competing four-electron pathways, leading to significantly higher H_2O_2 yields. These studies highlight that electronic modulation and pathway-selective ORR design are key to achieving efficient and stable H_2O_2 production (Table 2).

6.1.3. CO_2 reduction.

Effective CO_2 sequestration depends on the interrelated steps of catalytic reduction and adsorption, which are both controlled by surface chemistry and redox energetics, as various studies have highlighted. First, CO_2 is taken up *via* chemisorption, which includes amine acid–base interactions and metal–oxygen coordination.[107]

$$M\text{–}O + CO_2 \rightarrow M\text{–}O\text{–}COO^- \quad (12)$$

$$R\text{–}NH_2 + CO_2 \rightarrow R\text{–}NHCOO^- + H^+ \quad (13)$$

van der Waals and electrostatic forces result in weak physisorption. Lewis basic sites and porous architectures reduce the LUMO and facilitate electron absorption while increasing binding and causing the necessary linear curved distortion. To create the essential radical anion, activation happens *via* proton-coupled electron transfer (PCET).

$$CO_2 + e^- \rightarrow CO_2^{\bullet-} \quad (14)$$

Depending on the energetics of the catalyst band, the $CO_2^{\bullet-}$ intermediate directs several reduction pathways.

$$CO_2^{\bullet-} + H^+ + e^- \rightarrow HCOO^-(\text{Formate}) \quad (15)$$

$$CO_2^{\bullet-} + 2H^+ + 2e^- \rightarrow CO + H_2O(CO) \quad (16)$$

$$CO_2 + 6H^+ + 6e^- \rightarrow CH_3OH + H_2O\ (\text{methanol}) \quad (17)$$

$$CO_2 + 8H^+ + 8e^- \rightarrow CH_4 + 2H_2O\ (\text{methane}) \quad (18)$$

While N-rich MOF/ZIF-derived carbons and transition metals (Co, Ni, and Cu) stabilize intermediates through

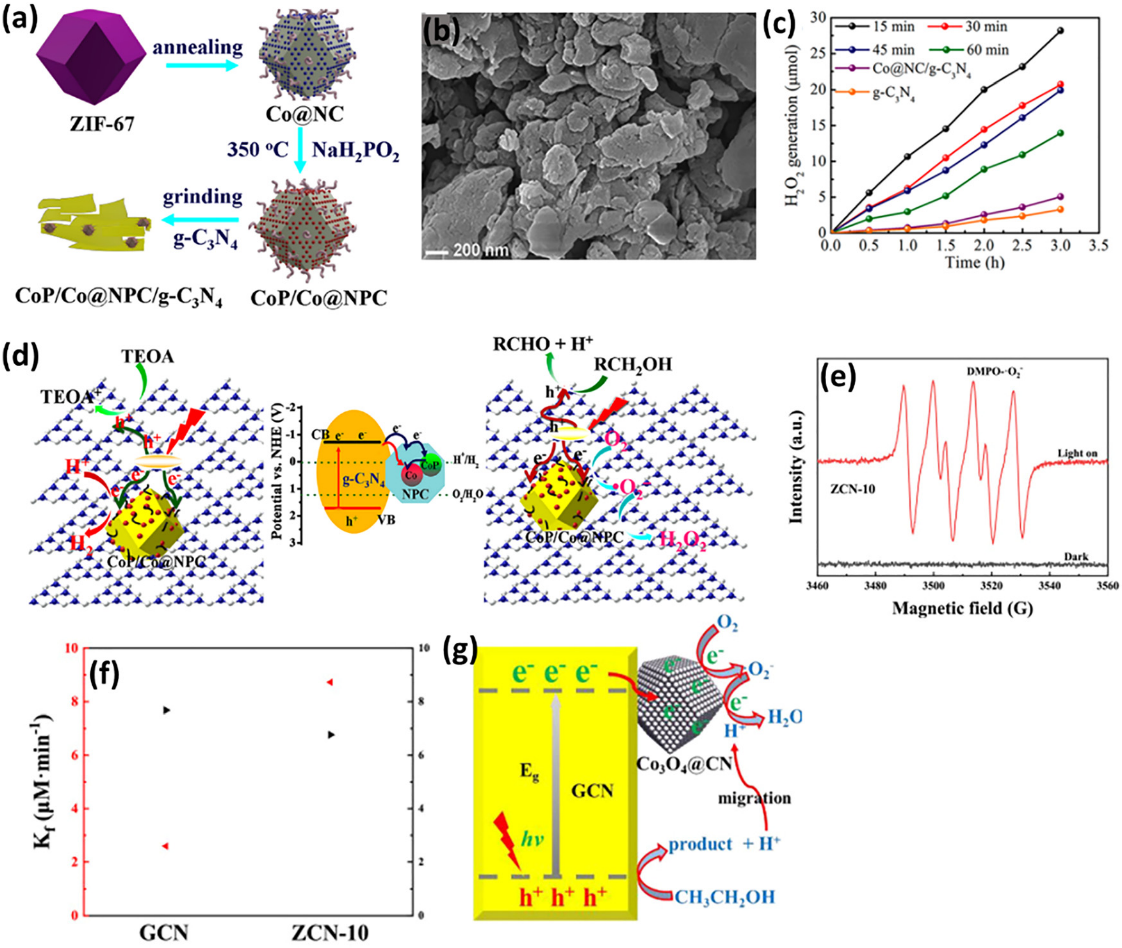

Fig. 15 (a) Schematic of CoP/Co@NPC/g-C_3N_4 photocatalyst preparation; adapted with permission from ref. 103 © 2020 the American Chemical Society. (b) SEM image of the CoP/Co@NPC-15/g-C_3N_4 photocatalyst; adapted with permission from ref. 103 © 2020 the American Chemical Society. (c) Production of H_2O_2 over Co@NC/g-C_3N_4 and CoP/Co@NPC/g-C_3N_4, following 15, 30, 45, and 60 minutes of phosphidation; adapted with permission from ref. 103 © 2020 the American Chemical Society. (d) Potential pathways for H_2 and H_2O_2 production and charge transfer across the CoP/Co@NPC/g-C_3N_4 photocatalyst; adapted with permission from ref. 103 © 2020 the American Chemical Society. (e) ESR spectrum of •O over ZCN-10; adapted with permission from ref. 104 © 2024 Elsevier B.V. (f) Comparison between the H_2O_2 formation rate constant (K) and the decomposition rate constant (K) for ZCN-10 and GCN; adapted with permission from ref. 104 © 2024 Elsevier B.V. (g) Schematic for photocatalytic H_2O_2 production over ZCN-10; adapted with permission from ref. 104 © 2024 Elsevier B.V.

Table 2 Comparative study of the generation of H_2O_2 by ZIF-67-based materials

Sl No.	Materials	Methods	H_2O_2 production rate (mol g_{cat}^{-1} h^{-1})	Ref.
1	Pd/ZIF-67(Fe_2Co_8)	Sol–gel	4.92	105
2	ZnCo-ZIFs	Sol–gel	4.35	106
3	Co_3O_4@CN	Sol–gel	2.6553	104

M–CO_2 or M–C interactions, enabling C–O bond cleavage, heterojunctions improve charge separation. Product selectivity depends on the reductant; carbon-free donors (H_2O, H_2) mostly produce C_1 species, whereas CH_4 or CH_3OH encourages C_2–C_3 coupling. Thus, the key to next-generation CO_2 valorization is dual-functional materials that combine strong catalytic PCET activity with high CO_2 affinity.[108,109]

Li *et al.*[110] designed a ZIF-67/$Ti_3C_2T_x$ MXene heterostructure to enhance photocatalytic CO_2 reduction (Fig. 16a). The conductive $Ti_3C_2T_x$ suppresses charge recombination in ZIF-67, improves visible light absorption, accelerates electron transfer, and promotes CO_2 activation, while ZIF-67 offers abundant adsorption sites. CO_2 adsorption energy analysis (Fig. 16b) shows strong binding on ZIF-67 (−0.74 eV), weak binding on $Ti_3C_2T_x$ (−0.34 eV), and an optimal intermediate value for the composite (−0.54 eV), enabling efficient activation without overbinding. Electron-density-deference mapping (Fig. 16c) reveals ~0.50 e accumulation on CO_2, confirming effective electron donation from $Ti_3C_2T_x$. Under illumination, the electrons generated in ZIF-67 rapidly transfer to MXene, suppressing recombination and driving CO_2 reduction *via* *COOH → *CHO → *OCH_3/*CH_3 pathways to produce CO, CH_4, and H_2 with good stability (Fig. 16d). The enhanced activity results

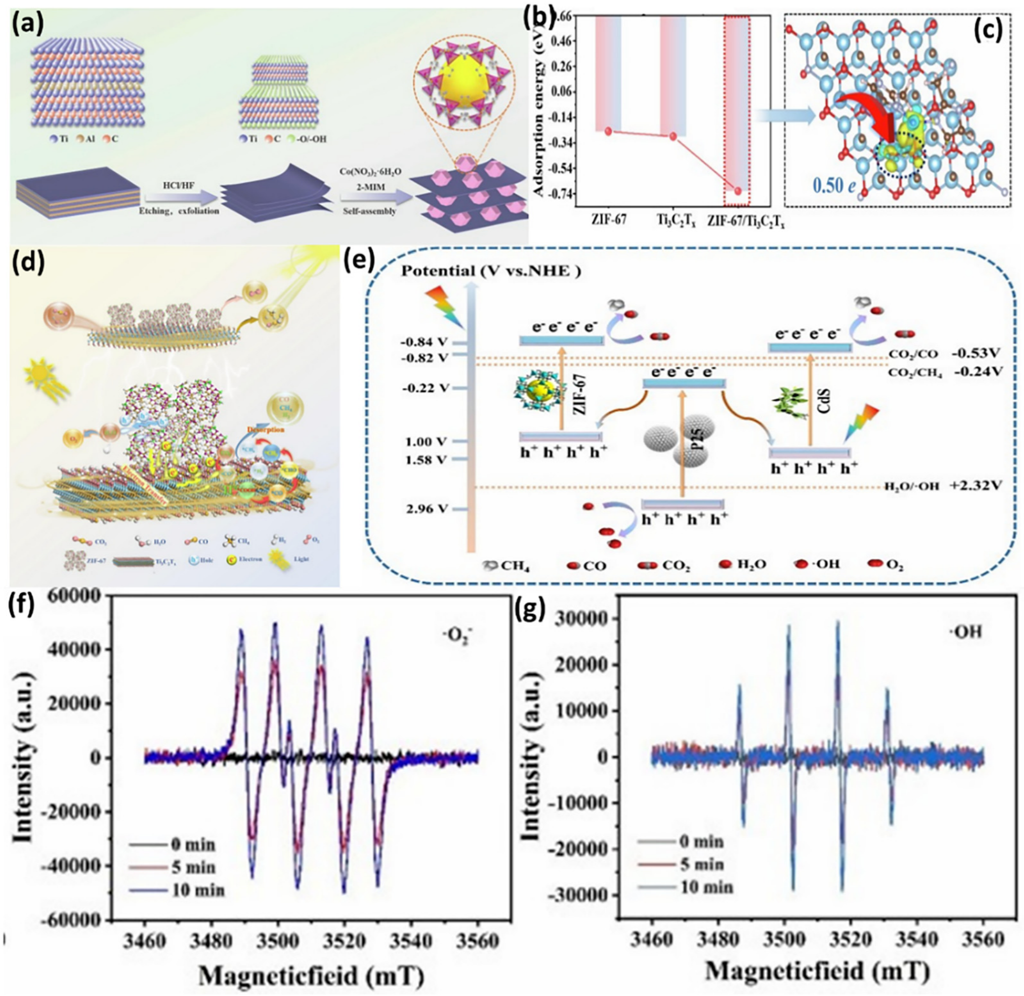

Fig. 16 (a) Schematic of the fabrication process of ZT-x; adapted with permission from ref. 110 © 2024 Elsevier B.V. (b) Comparison of the calculated CO_2 adsorption energies of ZIF-67, $Ti_3C_2T_x$, and ZIF-67/$Ti_3C_2T_x$; adapted with permission from ref. 110 © 2024 Elsevier B.V. (c) CO_2 adsorption structure and charge-density difference at ZIF-67/$Ti_3C_2T_x$; adapted with permission from ref. 110 © 2024 Elsevier B.V. (d) Mechanism diagram of photocatalytic CO_2RR based on *in situ* DRIFTS results over ZIF-67/$Ti_3C_2T_x$; adapted with permission from ref. 110 © 2024 Elsevier B.V. (e) Reaction mechanism diagram of the CdS-P25/ZIF-67 composite; adapted with permission from ref. 111 © 2022 Elsevier B.V. (f and g) ESR spectra of DMPO $O_2^{\bullet-}$ and DMP $OH^{\bullet}$ under light irradiation for CdS-P25/ZIF-67; adapted with permission from ref. 111 © 2022 Elsevier B.V.

from the synergy of strong CO_2 adsorption and efficient charge transport.

Wang *et al.*[111] prepared a CdS-P25/ZIF-67 composite *via* hydrothermal synthesis to enhance photocatalytic CO_2 reduction. Integrating visible light–responsive CdS and P25 with porous ZIF-67 improves solar absorption and charge separation. ZIF-67 acts as a light-harvesting, CO_2-adsorbing scaffold and catalytically activates CO_2 through Co^{2+} centres; CdS absorbs visible light, and P25 stabilizes charge transfer. A dual Z-scheme mechanism promotes efficient carrier separation and suppresses recombination (Fig. 16e). Characterizations confirm successful formation, XRD shows intact phases, SEM/TEM reveal uniform ZIF-67 coating, XPS identifies Co^{2+} active sites, UV-vis DRS and BET indicate enhanced light absorption and CO_2 adsorption, and PL and EIS confirm improved electron transfer. ESR analysis reveals the increasing concentrations of $O_2^{\bullet-}$ (Fig. 16f) and $^{\bullet}OH$ radicals (Fig. 16g) under irradiation, supporting active redox pathways.

In summary, CO_2 reduction over ZIF-67-based systems is enhanced by combining strong CO_2 adsorption with efficient charge separation through heterojunction engineering. Composites such as ZIF-67/$Ti_3C_2T_x$ and CdS-P25/ZIF-67 optimize CO_2 activation, accelerate electron transfer, and promote selective formation of CO and CH_4 *via* improved band alignment and radical-mediated pathways. These studies demonstrate that synergistic adsorption–transport coupling is essential for efficient solar-driven CO_2 conversion (Table 3).

6.2. Photocatalytic application

ZIF-67 is regarded as a promising photocatalytic material because of its high surface area, hierarchical porosity, and superior chemical stability, which collectively support strong adsorption and favourable surface kinetics. Despite these advantages, its wide bandgap constrains its solar-utilization efficiency. The formation of heterostructures with photoactive semiconductors substantially improves the performance of

Table 3 Comparative study of the reduction of CO_2 by ZIF-67-based composites

Sl No.	Materials	Methods	Production rate (μmol gcat^{-1})	Ref.
1	g-C_3N_4/ZIF-67	Sol–gel	325.5	112
2	ZIF-67	Sol–gel	37.4	71
3	ZIF-67-DCD-Ru	Hydrothermal	1495	113
4	GNF6/ZIF-67	Sol–gel	33.97	114
5	In_2O_3@ZIF-67	Solvothermal	33 420	115
6	ZIF-67@PPy	Sol–gel	1.49×10^4 (CO)	116
7	Au_{20}@ZIF-67	Solvothermal	2.5 (methanol) 0.5 (ethanol)	117
8	ZMO/Z67	Solvothermal	48.64 (methanol) 30.32 (ethanol)	118

ZIF-67 by promoting efficient charge-carrier separation, enhancing electron transport, and suppressing recombination. As a Co^{2+}-based MOF with imidazolate ligands, ZIF-67 follows semiconductor photocatalytic principles. Upon absorbing photons with energy greater than its bandgap, electron–hole pairs are generated as electrons transition from the valence band to the conduction band. These charge carriers drive redox reactions; conduction band electrons reduce O_2 to superoxide radicals ($O_2^{\bullet-}$), while valence band holes oxidize H_2O or OH^- to form hydroxyl radicals ($^{\bullet}OH$). These reactive oxygen species effectively degrade organic pollutants, such as dyes and antibiotics, as illustrated in Scheme 1.

6.2.1. Drug degradation. Photocatalytic antibiotic degradation is an effective method for removing pharmaceutical pollutants from water. It involves photon absorption, charge excitation, and surface reactions. Under visible light irradiation, electron–hole pairs are generated and migrate to the catalyst surface, where holes can directly oxidize antibiotic molecules. Two pathways operate simultaneously. In the reductive pathway, conduction band electrons reduce O_2 to $O_2^{\bullet-}$ (when the CB potential is more negative than −0.13 eV *vs.* RHE). In the oxidative pathway, valence band holes oxidize H_2O or OH^- to form $^{\bullet}OH$ (requiring potentials above +1.99 eV *vs.* RHE). The pH of the medium affects efficiency, as excess H^+ can promote charge recombination. The reactive species ($^{\bullet}OH$ and $O_2^{\bullet-}$) mineralize antibiotics into CO_2 and H_2O, while the simultaneous redox pathways suppress electron–hole recombination and enhance overall photocatalytic efficiency.[119–121]

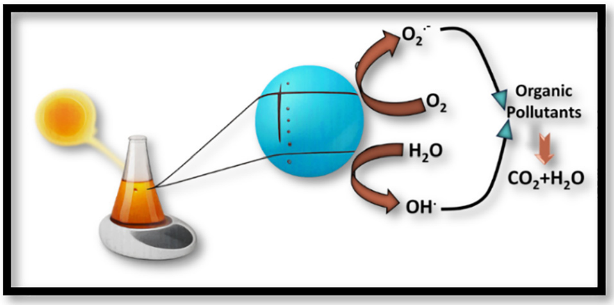

Scheme 1 Mechanism of photocatalysis of organic pollutants.

$$\text{Photocatalysis} \rightarrow \text{Photocatalysis} + h^+ + e^- \quad (19)$$

$$h^+ + \text{Drug} \rightarrow H_2O + CO_2 + \text{Degradation products} \quad (20)$$

$$O_2 + e^- \rightarrow O_2^{\bullet-} \quad (21)$$

$$H_2O/OH^- + h^+ \rightarrow OH^{\bullet} + H^+ \quad (22)$$

$$H^+ + e^- \rightarrow \text{energy} \quad (23)$$

$$\text{Drug} + OH^{\bullet}/O_2^{\bullet-} \rightarrow CO_2 + H_2O + \text{Degradation products} \quad (24)$$

Garg *et al.* (2025)[122] fabricated a WO_3@ZIF-67@ZIF-8 Z-scheme heterostructure for visible light–driven tetracycline degradation. The well-aligned heterojunction enables a direct Z-scheme pathway that enhances redox strength and suppresses charge recombination. Under illumination, electrons from the WO_3 conduction band recombine with holes in ZIF-67@ZIF-8, retaining the strong oxidative holes in WO_3 and high-energy electrons in ZIF-67@ZIF-8, which promote $^{\bullet}OH$ radical generation for TC degradation (Fig. 17a). The porous ZIF framework improves adsorption and charge transfer, while WO_3 enhances light absorption. The composite achieved 85.01% degradation in 120 min and after five consecutive cycles, the photocatalytic efficiency of WO_3@ZIF-67@ZIF-8 showed only a minor decrease of 4.61%, confirming its stability and effective MOF semiconductor band engineering.

Zhang *et al.* (2024)[123] demonstrated that incorporating β-cyclodextrin (β-CD) into Fe-doped ZIF-67 markedly enhances its PMS-based advanced oxidation. DFT results show that β-CD interacts with Fe@ZIF-67 mainly through hydrogen bonding, with the HOMO localized on the β-CD carbons and the LUMO delocalized (Fig. 17b), thereby stabilizing Fe centres, improving dispersion, and strengthening pollutant adsorption. The β-CD/Fe@ZIF-67 system achieved high degradation efficiencies toward PPCPs: 99.7% (CBZ), 91.3% (BPA), and 95.4% (DCF) (Fig. 17c), due to enhanced PMS activation and increased generation of reactive oxygen species. Scavenger and ESR analyses confirmed $SO_4^{\bullet-}$ and $^{\bullet}OH$ as dominant oxidants with pollutant-specific roles ($SO_4^{\bullet-}$ for CBZ and $O_2^{\bullet-}$ for DCF). Overall, β-CD acts as an effective molecular promoter, improving the MOF stability, adsorption, and ROS-driven pharmaceutical removal.

Wu *et al.* (2023)[124] reported the fabrication of a ZIF-67/BiOCl Z-scheme heterojunction, which greatly enhances the photocatalytic decomposition of organic pollutants under visible light irradiation. The principal innovation is the creation of a direct Z-scheme interface connecting n-type BiOCl with p-type ZIF-67, which increases the redox capacity by effectively separating photogenerated electrons and holes in space. Strong stability and recyclability were demonstrated by the composite, which retained around 79% activity after five cycles and achieved 97.4% RhB and 78.2% tetracycline degradations. The integration of ZIF-67 into BiOCl nanosheets was verified through structural analyses (XRD, FT-IR, SEM/TEM), which contributed to increased surface area and a greater number of catalytically active sites. Interfacial charge transfer and the existence of oxygen vacancies in BiOCl were demonstrated by

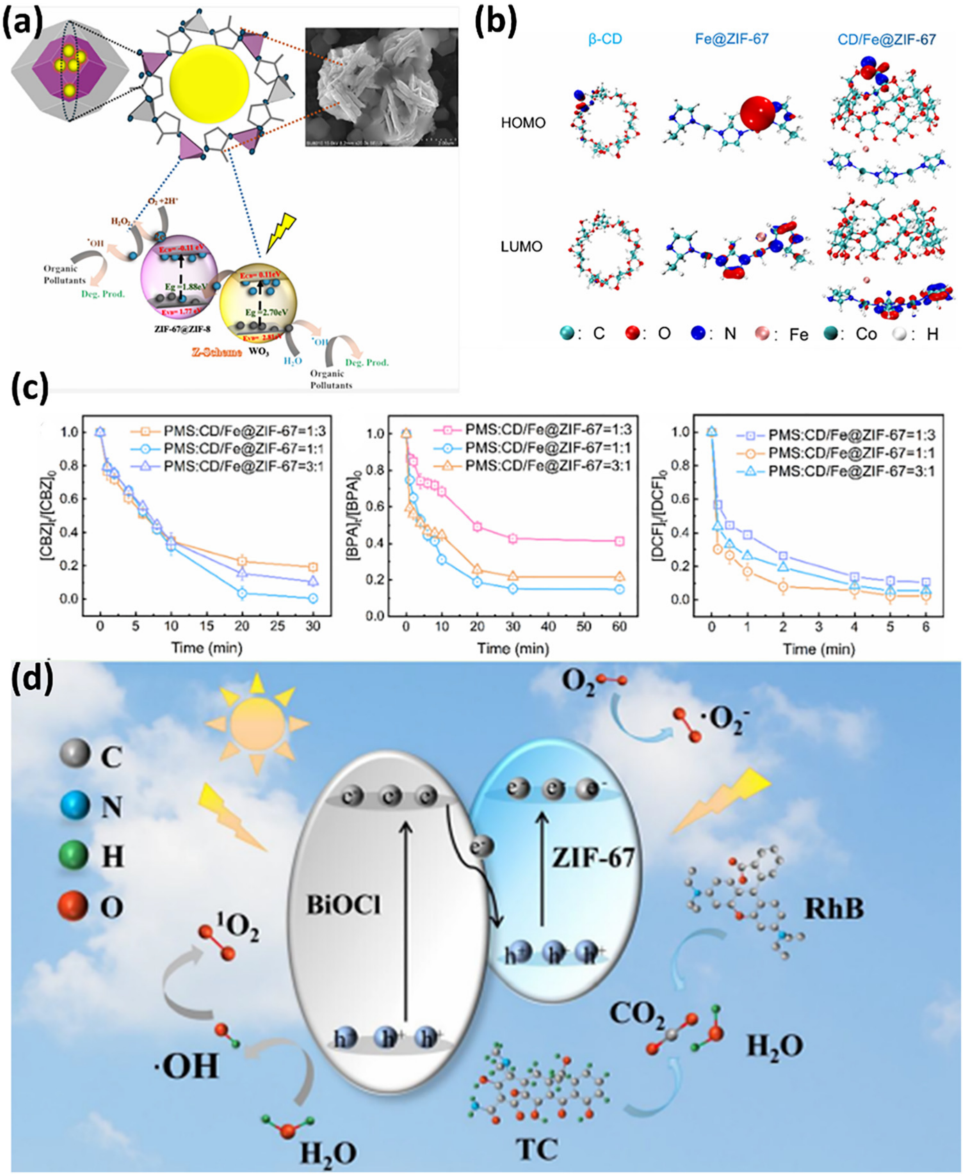

Fig. 17 (a) Photocatalytic Z-scheme mechanism. WO_3@ZIF-67@ZIF-8 degradation of organic pollutants; adapted with permission from ref. 122 © 2025 the American Chemical Society. (b) Optimized molecular structure, which includes the lowest unoccupied molecular orbital (LUMO) and the highest occupied molecular orbital (HOMO) iso-surfaces of the β-CD, Fe@ZIF-67, and CD/Fe@ZIF-67 molecules, was predicted computationally by DFT; adapted with permission from ref. 123 © 2024 the American Chemical Society. (c) Degradation ratios of CBZ, BPA, and DCF; adapted with permission from ref. 123 © 2024 the American Chemical Society; (d) and 15% ZIF-67/BiOCl photocatalytic mechanism is suggested for RhB and TC degradations; adapted with permission from ref. 124 © 2023 the American Chemical Society.

XPS, which improved photocatalysis. DRS and Mott–Schottky studies confirmed the Z-scheme charge-transfer mechanism (Fig. 17d).

In summary, ZIF-67 exhibits strong potential for photocatalytic drug degradation due to its high surface area and porosity, which facilitate efficient adsorption and surface reactions. Although its wide bandgap limits visible light absorption, coupling with suitable semiconductors significantly enhances charge separation and reactive-oxygen-species ($^{\bullet}OH$ and $O_2^{\bullet-}$) generation. Recent advances, including Z-scheme heterostructures (*e.g.* WO_3@ZIF-67@ZIF-8 and ZIF-67/BiOCl) and molecular modifications (β-CD/Fe@ZIF-67), demonstrate improved redox capability, stability, and degradation efficiency. Overall, band-structure engineering and interfacial optimization are key to advancing ZIF-67-based photocatalysts for effective drug removal (Table 4).

6.2.2. Dye degradation.

Dye removal from industrial effluents is a serious environmental issue due to their toxicity, ecological damage, and potential carcinogenic risks. Conventional treatment methods often fail to completely degrade dyes, leaving harmful by-products and generating excess sludge that leads to secondary pollution. Thus, efficient and eco-friendly technologies are urgently required to ensure complete degradation with minimal waste. Photocatalysis has emerged as a viable method for decomposing organic and hazardous pollutants in wastewater, as outlined in the reactions below.[129,130]

$$H_2O + h\nu \rightarrow HO^\bullet + H^\bullet \tag{25}$$

$$HO^\bullet + O_2 \rightarrow HO_2^\bullet \tag{26}$$

$$O_2 + e^- \rightarrow O_2^{\bullet-} \tag{27}$$

$$O_2^{\bullet-} + H^+ \rightarrow HO_2^\bullet \tag{28}$$

$$HO_2^\bullet + H^+ \rightarrow H_2O_2 \tag{29}$$

$$H_2O_2 \rightarrow 2HO^\bullet \tag{30}$$

The intermediate and final products are created when the dye reacts with an $HO^\bullet$ radical:

$$HO^\bullet + \text{dye} \rightarrow \text{intermediates} \rightarrow H_2O + CO_2 \tag{31}$$

Tran *et al.*[131] applied ZIF-67 for the visible light degradation of methyl orange (MO) (Fig. 18a and b). Hydrothermal synthesis produced highly crystalline rhombic dodecahedral particles ($\sim$600 nm) with exposed Co-N_4 active sites. Its microporous structure (0.65–0.95 nm) and high BET surface area (1398.9 $m^2\ g^{-1}$) enhance MO adsorption and diffusion. With a narrow bandgap ($\sim$1.91 eV), ZIF-67 achieved $>$88% MO degradation within 1 h. Visible light induces LMCT/MLCT transitions, generating electrons and holes that form $O_2^{\bullet-}$ and $^\bullet OH$ radicals. These reactive species oxidatively break MO azo bonds and aromatic rings, while the high porosity improves ROS transport and catalytic efficiency.

Li *et al.*[132] developed a multifunctional H-ZIF-67@PDA@-TiO_2 photocatalyst for visible light degradation of dyes (MO, CV, AF, CR, EB, RB). The structure integrates rhombic dodecahedral ZIF-67 with anatase TiO_2 *via* a $\sim$100 nm polydopamine (PDA) interlayer. SEM/TEM confirm the preservation of the ZIF-67 morphology and the successful TiO_2 grafting, while EDX/XPS, FTIR, and XRD verify the coexistence of ZIF-67 and anatase TiO_2 with characteristic chemical bonds. PDA enhances visible light absorption through its π-conjugated structure and facilitates rapid electron transport, suppressing recombination and improving quantum efficiency, compared to pure TiO_2. Under visible light, photoexcited charges migrate through PDA, generating $O_2^{\bullet-}$ (dominant) and $^\bullet OH$ radicals, as confirmed by ESR analysis (Fig. 18c). These reactive species oxidatively degrade and mineralize dyes into CO_2 and H_2O (Fig. 18d).

A magnetically recoverable Fe_3O_4@ZIF-67 nanocomposite designed for visible light–driven dye degradation was described by Guan *et al.* (2017).[133] According to SEM/TEM, the material was created at room temperature by coordinating Co^{2+} nodes with 2-methylimidazole around Fe_3O_4 seeds, resulting in a hierarchical flower-like design that improved interfacial charge transfer. While VSM showed superparamagnetic behaviour that allowed for quick magnetic recovery, XRD confirmed the coexistence of spinel Fe_3O_4 and crystalline ZIF-67 frameworks (Fig. 18e). Studies using radical trapping verified that h^+ and $O_2^{\bullet-}$ are the major reactive species. $O_2^{\bullet-}$ attacks azo (–N═N–) chromophores during the pseudo-first-order kinetics process of Congo Red degradation, resulting in progressive cleavage into smaller intermediates and ultimately mineralization to CO_2 and H_2O. Strong visible light absorption was detected by UV-vis DRS, which was ascribed to the charge transfer from the CO_2 ligand to the metal inside ZIF-67. Under illumination, amperometric *I–t* curves showed steady photocurrent production and quick charge-carrier response, suggesting effective electron separation. Because of its large surface area, the composite showed quick dye adsorption ($\sim$70% CR uptake in 30 min in the dark), followed by quicker photodegradation in the presence of light. Excellent recyclability was made possible by Fe_3O_4 inclusion, which sustained the performance for over five cycles (Fig. 18f). Fe_3O_4@ZIF-67 is a very promising photocatalyst for practical wastewater cleanup because of its high pollutant-degradation capacity, strong structural stability, and magnetic separability (Table 5). Recyclability is a crucial parameter for evaluating the practical applicability of ZIF-67-based photocatalysts. For instance, magnetic Fe_3O_4@ZIF-67 composites have demonstrated excellent stability during visible light–driven dye degradation, exhibiting nearly unchanged activity over five consecutive cycles (Fig. 18g). The catalyst was easily recovered *via* magnetic separation, and PXRD analysis confirmed the preservation of structural integrity after repeated use (Fig. 18h). These findings suggest that structural robustness and facile recovery strategies significantly enhance the reusability of ZIF-67-based systems, although long-term durability and metal leaching remain important considerations.

In summary, dye degradation using ZIF-67-based photocatalysts offers an efficient and sustainable alternative to conventional wastewater-treatment methods. Further performance enhancement is achieved through heterostructure engineering; for example, H-ZIF-67@PDA@TiO_2 composites exhibit improved light-absorption and charge-separation properties, and magnetically recoverable Fe_3O_4@ZIF-67 systems enable efficient degradation, along with easy recyclability.

Table 4 Comparative study of the degradation of antibiotics by ZIF-67-based materials

S. no.	Materials	Drug	Degradation efficiency (%)	Ref.
1	MoS_2@ZIF-67	TC	72	125
2	ZIF-67	TC	82	126
3	ZIF-8@ZIF-67	Capecitabine 5-Fluorouracil	98.4 97.4	127
4	ZIF-8@ZIF-67	Ciprofloxacin levofloxacin ofloxacin	65 54 48	128
5	ZIF-67/BiOCl	TC	78.2	124

7. Future Work

However, because ZIF-67 composite materials are currently expensive, more studies are required to make them feasible

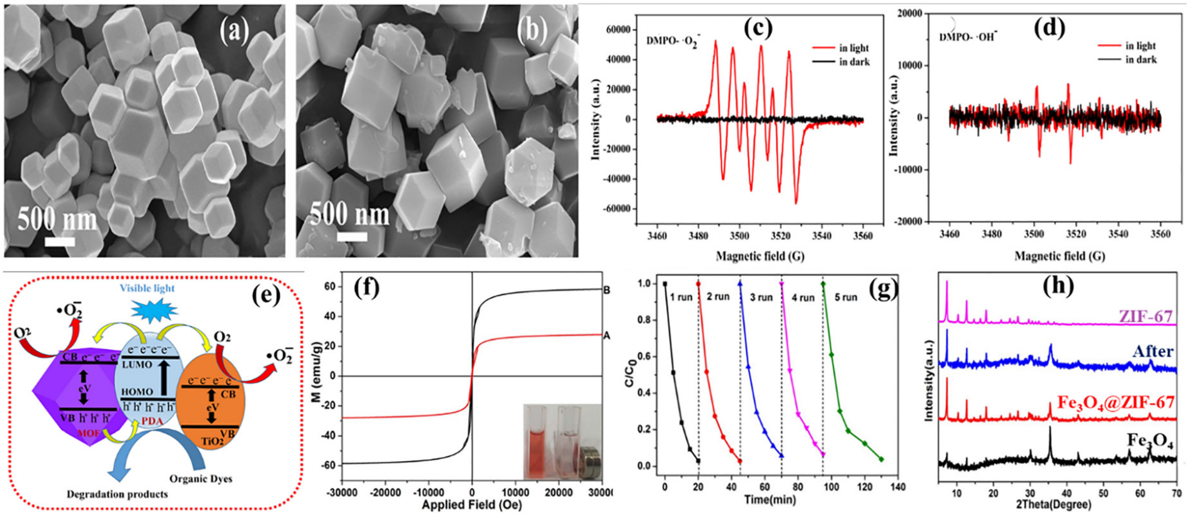

Fig. 18 SEM images of the ZIF-67 nanoparticles (a) before and (b) after three cycles of MO photodegradation; adapted with permission from ref. 131 © 2021 Elsevier Inc. ESR spectra of the H-ZIF-67@PDA@TiO_2 hybrids; (c) DMPO $O_2^{\bullet -}$ radical species were detected in methanol, and (d) DMPO $OH^{\bullet}$ radical species were detected in deionized water; adapted with permission from ref. 132 © 2021 Elsevier B.V. (e) Suggested photocatalytic reaction mechanism over H-ZIF-67@PDA@TiO_2 hybrids when exposed to visible light; adapted with permission from ref. 133 © 2017 Elsevier Inc. (f) Fe_3O_4 powder and Fe_3O_4@ZIF-67 magnetic hysteresis loop measurements (inset: sample separation from solution under an external magnetic field); adapted with permission from ref. 133 © 2017 Elsevier Inc. (g) Five repeated processes of using Fe_3O_4@ZIF-67 for the photodegradation of CR under visible light irradiation; (h) XRD pattern of Fe_3O_4, as-synthesized Fe_3O_4@ZIF-67, Fe_3O_4@ZIF-67 after reaction, and ZIF-67 adapted with permission from ref. 133 © 2017 Elsevier Inc.

Table 5 Comparative study of the degradation of dye by ZIF-67-based materials

S. no.	Materials	Dye	% of degradation	pH	References
1	Fe_3O_4@ZIF-67	Congo red	70	12	133
2	$Zn_{0.2}Cd_{0.8}S$@ZIF-67	Rhodamine B	98.4	8	134
3	GO/ZIF-67 Ni/ZIF-67	Crystal violet	99.9	4	135
4	ZIF-67@ZIF-11	MB	95	8	136
5	ZIF-67	MO	88	9	131

for widespread photocatalytic applications. We think that researchers have only just begun fully investigating the potential of ZIF-67. The following premises form the basis of our reasoning:

- ZIF-67-based materials should be produced on a large scale by methodically investigating innovative and effective synthetic techniques. A special focus should be placed on creating economical, environmentally friendly, and sustainable methods that do not require costly or hazardous solvents. This will enable scalable synthesis while preserving the functional properties and structural integrity of the final product.
- *In situ* operando characterization techniques should be employed to elucidate charge-transfer dynamics and active-site evolution during photocatalytic operations. Computational modelling (*e.g.*, DFT calculations) can guide rational band-structure and interface designs. The integration of ZIF-67-based materials into functional reactors, devices, or photoelectrochemical systems should be explored. Life cycle assessment and ecotoxicity evaluation are essential to ensure environmental safety and economic viability.
- The majority of ZIF-67-derived materials possess pore sizes smaller than 2 nm, rendering them microporous. Due to steric hindrance, this may reduce their effectiveness, particularly when used for larger pollutant molecules. For enhanced photocatalytic performance, it is desirable to engineer ZIF-67 with hierarchical porosity, combining macropores, mesopores, and micropores.
- In order to successfully integrate ZIF-67-based materials into industrial applications, their long-term stability is still a crucial issue that needs to be resolved. Enhancing their mechanical, chemical, and thermal stability should receive special attention, particularly under demanding or changing operating conditions. Such robustness is necessary to preserve their overall performance, catalytic activity, and structural integrity over extended use, increasing their usefulness in actual processes.
- ZIF-67 derivatives outperform pristine ZIF-67, mostly because of the mutually beneficial interactions between their components. Improving the functional performance and expanding the applicability of ZIF-67 derivatives require careful design and synthesis of materials with controllable morphology and porosity based on the parent ZIF-67 structure.
- The synthesis of ZIF-67 with high crystallinity and uniform particle size remains challenging, despite numerous advances in fabrication methods for research and scale-up. Achieving such uniformity is vital for achieving optimal functionality, particularly in compact devices and electron-transport applications.

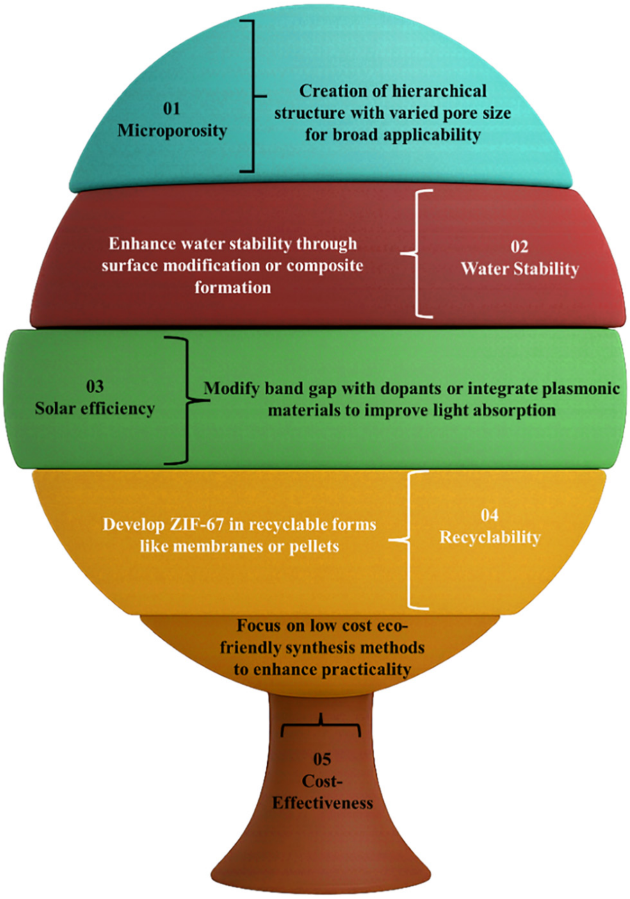

Fig. 19 Schematic of challenges and future research directions towards ZIF-67-based nanomaterials for photocatalytic application.

- ZIF-67-based materials are usually produced as loose powders; thus, they can cause problems in industrial processes, including dust production, abrasion, clogging, and pressure drop. Thus, forming these materials into monolithic or structured shapes ought to be viewed as a viable approach to resolving these issues and enhancing their usefulness in large-scale operations.
- Owing to the water sensitivity of its coordination bonds, ZIF-67 shows comparatively low water stability. Cost-effectively enhancing ZIF-67's long-term water stability is still a major hurdle.
- For industrial applications, the chemical and thermal stability of ZIF-67-based composites needs to be carefully tuned. To increase their efficacy, the catalytic sites and porosity must also be carefully regulated.
- The majority of the studies on materials based on ZIF-67 have so far only been conducted at the laboratory level. Cost-effectiveness and industrial viability aspects that are frequently disregarded need to be given more attention for successful translation into real-world applications. Although the quick development of ZIF-67-based materials presents encouraging opportunities for further technological advancements, ongoing research and development are necessary to close the gap between lab work and widespread commercial application.
- Lastly, the creation of environmentally friendly ZIF-67-based materials is necessary for their extensive use in fields like water treatment and energy generation. In practical terms, it is crucial to incorporate environmentally friendly features. In order to ensure environmental safety and economic feasibility for large-scale implementation, future research should focus on designing economical synthesis routes that use sustainable and biocompatible components (Fig. 19).

The ultimate goal of this field is to bridge the gap between fundamental ZIF-67 material research and its practical, large-scale deployment in real-world environmental and energy applications.

8. Conclusion

ZIF-67 has attracted a lot of attention due to its promising properties, despite the fact that ZIFs have only recently emerged. The remarkable catalytic activity, high surface area, and adjustable porosity of ZIF-67-based materials have led to their increased use in environmental remediation and energy generation. This review highlights the synthesis methodologies, prominent features, and light-driven applications of ZIF-67-based photocatalysts and their composite systems, including for pollutant removal, CO_2 reduction, H_2 evolution, and H_2O_2 production. The remarkable adaptability and efficacy of ZIF-67 composites in these domains underscore their noteworthy potential to propel sustainable technological advancements. The exceptional qualities of ZIF-67, including its stable porosity, large number of active sites, and effective charge separation, make it a promising catalyst in the field of materials science. Compared to the materials obtained by conventional single-catalyst methods, catalyst composites developed by combining ZIF-67 with additional functional materials offer improved performance in a number of photocatalytic applications. The ability of ZIF-67 to absorb solar light is enhanced by the photoactive semiconductors or molecules present in the composite. High-surface-area ZIF-67-based composites offer a large number of active sites, inhibit nanoparticle aggregation, and act as electron acceptors to effectively separate charge carriers. ZIF-67 and semiconductors undergo strong interfacial interactions that improve electron transfer and visible light harvesting, resulting in noticeably higher photocatalytic efficiency. The development of ZIF-67-based photocatalysts for energy production and environmental remediation is gaining traction because of their affordability, environmental sustainability and stability in complex environments.

Author contributions

Monalisa Samal: conceptualization, writing – original draft, methodology, investigation and data curation. Binita Nanda: supervision, conceptualization, validation, review and editing.

Conflicts of interest

There are no conflicts to declare.

Data availability

This review article synthesizes and discusses data that have already been published and are publicly available from the sources cited within the manuscript. No new data were generated during the preparation of this review. All data supporting the findings of this study can be accessed through the relevant references provided in the manuscript.

Acknowledgements

The authors express their profound gratitude toward Siksha 'O' Anusandhan (Deemed to be University).

References

1 M. S. Rahaman, H. Thérien-Aubin, M. Ben-Sasson, C. K. Ober, M. Nielsen and M. Elimelech, *J. Mater. Chem. B*, 2014, **2**, 1724–1732.
2 S. Bolisetty, M. Peydayesh and R. Mezzenga, *Chem. Soc. Rev.*, 2019, **48**, 463–487.
3 V. Hasija, A. Sudhaik, P. Raizada, A. Hosseini-Bandegharaei and P. Singh, *J. Environ. Chem. Eng.*, 2019, **7**, 103272.
4 S. Patial, V. Hasija, P. Raizada, P. Singh, A. A. P. K. Singh and A. M. Asiri, *J. Environ. Chem. Eng.*, 2020, **8**, 103791.
5 P. Thakur, P. Raizada, P. Singh, A. Kumar, A. A. P. Khan and A. M. Asiri, *Arab. J. Chem.*, 2020, **13**, 8271–8300.
6 K. Sharma, P. Raizada, A. Hosseini-Bandegharaei, P. Thakur, R. Kumar, V. K. Thakur, V.-H. Nguyen and S. Pardeep, *Process Saf. Environ. Prot.*, 2020, **142**, 63–75.
7 H. Choi, E. Stathatos and D. D. Dionysiou, *Desalination*, 2007, **202**, 199–206.
8 M. A. Shannon, P. W. Bohn, M. Elimelech, J. G. Georgiadis, B. J. Mariñas and A. M. Mayes, *Nature*, 2008, **452**, 301–310.
9 P. Raizada, S. Sharma, A. Kumar, P. Singh, A. A. P. Khan and A. M. Asiri, *J. Environ. Chem. Eng.*, 2020, **8**, 104230.
10 H. Huang, L. Jiang, J. Yang, S. Zhou, X. Yuan, J. Liang, H. Wang, H. Wang, Y. Bu and H. Li, *Renewable Sustainable Energy Rev.*, 2023, **173**, 113110.
11 J. Yang, H. Wang, L. Jiang, H. Yu, Y. Zhao, H. Chen, X. Yuan, J. Liang, H. Li and Z. Wu, *Chem. Eng. J.*, 2022, **427**, 130991.
12 A. Mishra, N. Priyadarshini, S. Mansingh and K. Parida, *Adv. Colloid Interface Sci.*, 2024, 103300.
13 J. Sahu, D. Prusty, S. Mansingh and K. Parida, *Int. J. Hydrogen Energy*, 2023, **48**, 29097–29118.
14 S. Tuckute, S. Varnagiris, M. Urbonavicius, M. Lelis and S. Sakalauskaitea, *Appl. Surf. Sci.*, 2019, **489**, 576–583.
15 H. Yi, M. Yan, D. Huang, G. Zeng, C. Lai, M. Li, X. Huo, L. Qin, S. Liu and X. Liu, *et al.*, *Appl. Catal., B*, 2019, **250**, 52–62.
16 M. W. Kadi, R. M. Mohamed and A. A. Ismail, *Ceram. Int.*, 2020, **46**, 8819–8826.
17 S. Sa-nguanprang, A. Phuruangrat, T. Thongtem and S. Thongtem, *Inorg. Chem. Commun.*, 2020, **117**, 107944.
18 K. S. Bhavsar, P. K. Labhane, R. B. Dhake and G. H. Sonawane, *Chem. Phys. Lett.*, 2020, **744**, 137202.
19 G.-J. Lee and J. J. Wu, *Powder Technol.*, 2017, **318**, 8–22.
20 S. B. Atla, W.-R. Lin, T.-C. Chien, M.-J. Tseng, J.-C. Shu, C.-C. Chen and C.-Y. Chen, *Mater. Chem. Phys.*, 2018, **216**, 380–386.
21 J. Carbajo, M. Jiménez, S. Miralles, S. Malato, M. Faraldos and A. Bahamonde, *Chem. Eng. J.*, 2016, **291**, 64–73.
22 V. Dutta, S. Sharma, P. Raizada, A. Hosseini-Bandegharaei, V. K. Gupta and P. Singh, *et al.*, *J. Saudi Chem. Soc.*, 2019, **23**, 1119–1136.
23 Y. Li, H. Xu, S. Ouyang and J. Ye, *Phys. Chem. Chem. Phys.*, 2016, **18**, 7563–7572.
24 S. Sanati, D. B. Cordes, A. M. Z. Slawin, J. Qian and R. Abazari, *Inorg. Chem.*, 2024, **64**, 510–518.
25 E. Safaralizadeh, S. J. Darzi, A. R. Mahjoub and R. Abazari, *Res. Chem. Intermed.*, 2017, **43**, 1197–1209.
26 R. Abazari, Z. Ahmadi Torkamani, A. Ejsmont, A. Krawczuk, J. Goscianska, R. S. Varma and S. Sanati, *Inorg. Chem.*, 2025, **64**, 361–370.
27 O. M. Yaghi, G. Li and H. Li, *Nature*, 1995, **378**, 703–706.
28 A. Phan, C. J. Doonan, F. J. Uribe-Romo, C. B. Knobler, M. O'keeffe and O. M. Yaghi, *Acc. Chem. Res.*, 2009, **43**(1), DOI: 10.1021/ar900116g.
29 O. M. Yaghi, M. O'Keeffe, N. W. Ockwig, H. K. Chae, M. Eddaoudi and J. Kim, *Nature*, 2003, **423**, 705–714.
30 K. Li, Y. Zhang, Y.-Z. Lin, K. Wang and F.-T. Liu, *ACS Appl. Mater. interfaces*, 2019, **11**, 28918–28927.
31 J. Ran, H. Zeng, J. Cai, P. Jiang, P. Yan, L. Zheng, Y. Bai, X. Shen, B. Shi and H. Tong, *Chem. Eng. J.*, 2018, **333**, 20–33.
32 Y. Liu, Z. Zhu, X. Pei, X. Zhang, X. Cheng, S. Hu, X. Gao, J. Wang, J. Chen and Q. Wan, *ACS Appl. Mater. Interfaces*, 2020, **12**, 36978–36995.
33 M. Ahmad, M. Yousaf, W. Cai and Z.-P. Zhao, *Chem. Eng. J.*, 2023, **453**, 139846.
34 X. Li, Y. Liu, J. Wang, J. Gascon, J. Li and B. der Bruggen, *Chem. Soc. Rev.*, 2017, **46**, 7124–7144.
35 J. Li, X. Wang, G. Zhao, C. Chen, Z. Chai, A. Alsaedi, T. Hayat and X. Wang, *Chem. Soc. Rev.*, 2018, **47**, 2322–2356.
36 X. Xu, H. Wang, J. Liu and H. Yan, *J. Mater. Sci.: Mater. Electron.*, 2017, **28**, 7532–7543.
37 F. Song, Y. Cao, Y. Zhao, R. Jiang, Q. Xu, J. Yan and Q. Zhong, *J. Nanomater.*, 2020, **2020**, 1508574.
38 K. S. Park, Z. Ni, A. P. Côté, J. Y. Choi, R. Huang, F. J. Uribe-Romo, H. K. Chae, M. O'Keeffe and O. M. Yaghi, *Proc. Natl. Acad. Sci U. S. A.*, 2006, **103**, 10186–10191.
39 Y. Pan, Y. Liu, G. Zeng, L. Zhao and Z. Lai, *Chem. Commun.*, 2011, **47**, 2071–2073.
40 C. Duan, Y. Yu, F. Li, Y. Wu and H. Xi, *CrystEngComm*, 2020, **22**, 2675–2680.
41 L. Qin, Y. Li, F. Liang, L. Li, Y. Lan, Z. Li, X. Lu, M. Yang and D. Ma, *Microporous Mesoporous Mater.*, 2022, **341**, 112098.
42 S. M. Mousavi, S. A. Hashemi, S. Bahrani, S. Mosleh, W.-H. Chiang, K. Yousefi, S. Ramakrishna, L. C. Wei and

N. Omidifar, *Environ. Sci. Pollut. Res.*, 2022, **29**, 56055–56067.

43 N. Cheng, L. Ren, X. Xu, Y. Du and S. X. Dou, *Adv. Energy Mater.*, 2018, **8**, 1801257.

44 Y. Liu, H. Cheng, M. Cheng, Z. Liu, D. Huang, G. Zhang, B. Shao, Q. Liang, S. Luo and T. Wu, *et al.*, *Chem. Eng. J.*, 2021, **417**, 127914.

45 X. Huang, J. Zhang and X. Chen, *Chin. Sci. Bull.*, 2003, **48**, 1531–1534.

46 Y.-Q. Tian, C.-X. Cai, Y. Ji, X.-Z. You and G.-H. Lee, *Angew. Chem., Int. Ed.*, 2002, **114**(8), 1442–1444.

47 Y.-Q. Tian, C.-X. Cai, X.-M. Ren, C.-Y. Duan, Y. Xu, S. Gao and X.-Z. You, *Chem. – Eur. J.*, 2003, **9**, 5673–5685.

48 L. Zhang, A. Wu, M. Tian, Y. Xiao, X. Shi, H. Yan, C. Tian and H. Fu, *Chem. Commun.*, 2018, **54**, 11088–11091.

49 X. Ma, Y.-X. Zhou, H. Liu, Y. Li and H.-L. Jiang, *Chem. Commun.*, 2016, **52**, 7719–7722.

50 S. Dang, Q.-L. Zhu and Q. Xu, *Nat. Rev. Mater.*, 2017, **3**, 1–14.

51 X. Cao, C. Tan, M. Sindoro and H. Zhang, *Chem. Soc. Rev.*, 2017, **46**, 2660–2677.

52 Y. Dou, J. Zhou, F. Yang, M.-J. Zhao, Z. Nie and J.-R. Li, *J. Mater. Chem. A*, 2016, **4**, 12526–12534.

53 L. Wang, H. Zhu, Y. Shi, Y. Ge, X. Feng, R. Liu, Y. Li, Y. Ma and L. Wang, *Nanoscale*, 2018, **10**, 11384–11391.

54 S. Gao, Y. Han, M. Fan, Z. Li, K. Ge, X.-J. Liang and J. Zhang, *Sci. China Mater.*, 2020, **63**, 2429–2434.

55 R. Liu, B. Wu, R. Liu, X. Zhang, Y. Sun and J. Ma, *Microchem. J.*, 2025, **212**, 113510.

56 A. Zhou, Y. Dou, C. Zhao, J. Zhou, X.-Q. Wu and J.-R. Li, *Appl. Catal., B*, 2020, **264**, 118519.

57 C. Duan, Y. Yu and H. Hu, *Green Energy Environ.*, 2022, **7**, 3–15.

58 X. Yang, B. Tan, B. Wang, L. Yao, X. Li, D. Zhao, W. Li, L. Cao, Y. Huang and X. Wang, *Molecules*, 2022, **27**, 8370.

59 P. Krokidas, M. Castier, S. Moncho, D. N. Sredojevic, E. N. Brothers, H. T. Kwon, H.-K. Jeong, J. S. Lee and I. G. Economou, *J. Phys. Chem. C*, 2016, **120**, 8116–8124.

60 X. Feng and M. A. Carreon, *J. Cryst. Growth*, 2015, **418**, 158–162.

61 C. Jiang and B. Wen, *J. Mater. Sci.: Mater. Electron.*, 2022, **33**, 5730–5749.

62 J. Cravillon, C. A. Schröder, R. Nayuk, J. Gummel, K. Huber and M. Wiebcke, *Angew. Chem., Int. Ed.*, 2011, **50**, 8067–8071.

63 H. Zhou, W. Cao, N. Sun, L. Jiang, Y. Liu and H. Pang, *Chin. Chem. Lett.*, 2021, **32**, 3123–3127.

64 X. Feng, T. Wu and M. A. Carreon, *J. Cryst. Growth*, 2016, **455**, 152–156.

65 V.-A. Thai, T.-B. Nguyen, C.-W. Chen, C. P. Huang, R. Doong, L. Chen and C.-D. Dong, *Sep. Purif. Technol.*, 2024, **334**, 126033.

66 W. Zhu, Y. Wu, G. Yi, X. Su, Q. Pan, S. Shi, O. Oderinde, G. Xiao, C. Zhang and Y. Zhang, *J. Ind. Eng. Chem.*, 2023, **119**, 274–285.

67 M. Hu, D. Zhao, X. Yan, Y. Wang, J. Zhang, X. Hu, M. Zhou and P. Liu, *Appl. Catal., B*, 2025, **362**, 124753.

68 Z. Naghshbandi, K. Moradi, A. Salimi, M. Gholinejad and A. Feizabadi, *Electrochim. Acta*, 2024, **479**, 143884.

69 Z. Shi, Y. Yu, C. Fu, L. Wang and X. Li, *RSC Adv.*, 2017, **7**, 29227–29232.

70 J. Ethiraj, S. Palla and H. Reinsch, *Microporous Mesoporous Mater.*, 2020, **294**, 109867.

71 J. Qin, S. Wang and X. Wang, *Appl. Catal., B*, 2017, **209**, 476–482.

72 L. Wang, B. Wen, X. Bai, C. Liu and H. Yang, *J. Colloid Interface Sci.*, 2019, **540**, 30–38.

73 C. Duan, Y. Yu, P. Yang, X. Zhang, F. Li, L. Li and H. Xi, *Ind. Eng. Chem. Res.*, 2019, **59**, 774–782.

74 C. Duan, Y. Yu, J. Xiao, X. Zhang, L. Li, P. Yang, J. Wu and H. Xi, *Sci. China Mater.*, 2020, **63**, 667–685.

75 R. R. Kuruppathparambil, T. Jose, R. Babu, G.-Y. Hwang, A. C. Kathalikkattil, D.-W. Kim and D.-W. Park, *Appl. Catal., B*, 2016, **182**, 562–569.

76 J. Zhang, T. Zhang, D. Yu, K. Xiao and Y. Hong, *CrystEngComm*, 2015, **17**, 8212–8215.

77 C. Avci, J. Ariñez-Soriano, A. Carné-Sánchez, V. Guillerm, C. Carbonell, I. Imaz and D. Maspoch, *Angew. Chem.*, 2015, **127**, 14625–14629.

78 W. Li, K. Wang, X. Yang, F. Zhan, Y. Wang, M. Liu, X. Qiu, J. Li, J. Zhan and Q. Li, *et al.*, *Chem. Eng. J.*, 2020, **379**, 122256.

79 C. Duan, F. Li, M. Yang, H. Zhang, Y. Wu and H. Xi, *Ind. Eng. Chem. Res.*, 2018, **57**, 15385–15394.

80 Q. Yang, R. Lu, S. Ren, C. Chen, Z. Chen and X. Yang, *Chem. Eng. J.*, 2018, **348**, 202–211.

81 L. Xu, Y. Xiong, B. Dang, Z. Ye, C. Jin, Q. Sun and X. Yu, *Mater. Des.*, 2019, **182**, 108006.

82 N. M. Mahmoodi, M. Taghizadeh, A. Taghizadeh, J. Abdi, B. Hayati and A. A. Shekarchi, *Appl. Surf. Sci.*, 2019, **480**, 288–299.

83 N. T. T. Tu, P. C. Sy, T. V. Thien, T. T. T. Toan, N. H. Phong, H. T. Long and D. Q. Khieu, *J. Mater. Sci.*, 2019, **54**, 11654–11670.

84 F. Hillman, J. M. Zimmerman, S.-M. Paek, M. R. A. Hamid, W. T. Lim and H.-K. Jeong, *J. Mater. Chem. A*, 2017, **5**, 6090–6099.

85 P. A. Julien, C. Mottillo and T. Friščić, *Green Chem.*, 2017, **19**, 2729–2747.

86 C. Mottillo, Y. Lu, M.-H. Pham, M. J. Cliffe, T.-O. Do and T. Friščić, *Green Chem.*, 2013, **15**, 2121–2131.

87 M. Krishtab, I. Stassen, T. Stassin, A. J. Cruz, O. O. Okudur, S. Armini, C. Wilson, S. De Gendt and R. Ameloot, *Nat. Commun.*, 2019, **10**, 3729.

88 I. Stassen, M. Styles, G. Grenci, H. Van Gorp, W. Vanderlinden, S. De Feyter, P. Falcaro, D. De Vos, P. Vereecken and R. Ameloot, *Nat. Mater.*, 2016, **15**, 304–310.

89 X.-D. Du, C.-C. Wang, J.-G. Liu, X.-D. Zhao, J. Zhong, Y.-X. Li, J. Li and P. Wang, *J. Colloid Interface Sci.*, 2017, **506**, 437–441.

90 W. Sun, X. Zhai and L. Zhao, *Chem. Eng. J.*, 2016, **289**, 59–64.
91 X. Fang, Q. Shang, Y. Wang, L. Jiao, T. Yao, Y. Li, Q. Zhang, Y. Luo and H.-L. Jiang, *Adv. Mater.*, 2018, **30**, 1705112.
92 C. Acar, I. Dincer and G. F. Naterer, *Int. J. Energy Res.*, 2016, **40**, 1449–1473.
93 Y. Li, Z. Jin and T. Zhao, *Chem. Eng. J.*, 2020, **382**, 123051.
94 S. Khan, T. Noor, N. Iqbal, E. Pervaiz and L. Yaqoob, *RSC Adv.*, 2023, **13**, 24973–24987.
95 D. You, D. Shi, Q. Cheng, Y. Chen and Z. Pan, *Environ. Sci.: Nano*, 2020, **7**, 2809–2822.
96 H. Gong, X. Zhang, G. Wang, Y. Liu, Y. Li and Z. Jin, *Mol. Catal.*, 2020, **485**, 110832.
97 Y. Zhang and Z. Jin, *J. Phys. Chem. C*, 2019, **123**, 18248–18263.
98 Y. Zhang, H. Liu, P. Zhu, M. Yang and Z. Jin, *Int. J. Hydrogen Energy*, 2023, **48**, 32631–32641.
99 K. C. Devarayapalli, S. V. P. Vattikuti, T. V. M. Sreekanth, K. S. Yoo, P. C. Nagajyothi and J. Shim, *Appl. Organomet. Chem.*, 2020, **34**, e5376.
100 S. Kato, J. Jung, T. Suenobu and S. Fukuzumi, *Energy Environ. Sci.*, 2013, **6**, 3756–3764.
101 Y. Xie, Y. Li, Z. Huang, J. Zhang, X. Jia, X.-S. Wang and J. Ye, *Appl. Catal., B*, 2020, **265**, 118581.
102 H. Hirakawa, S. Shiota, Y. Shiraishi, H. Sakamoto, S. Ichikawa and T. Hirai, *ACS Catal.*, 2016, **6**, 4976–4982.
103 Q. Ji, L. Pan, J. Xu, C. Wang and L. Wang, *ACS Appl. Nano Mater.*, 2020, **3**, 3558–3567.
104 H. Chen, L. Nie, Y. Yang, C. Fang, X. Chen and X. Li, *Mol. Catal.*, 2024, **569**, 114584.
105 V. L. N. Vo, K. Yu and Y.-M. Chung, *Catal. Today*, 2025, 115533.
106 C. Zhang, L. Yuan, C. Liu, Z. Li, Y. Zou, X. Zhang, Y. Zhang, Z. Zhang, G. Wei and C. Yu, *J. Am. Chem. Soc.*, 2023, **145**, 7791–7799.
107 R. N. Compton, P. W. Reinhardt and C. D. Cooper, *Collisional ionization of Na, K, and Cs by CO $$ sub 2$$, COS, and CS $$ sub 2$$: molecular electron affinities*, 1975.
108 J. Mao, T. Peng, X. Zhang, K. Li and L. Zan, *Catal. Commun.*, 2012, **28**, 38–41.
109 C.-C. Yang, J. Vernimmen, V. Meynen, P. Cool and G. Mul, *J. Catal.*, 2011, **284**, 1–8.
110 Z. Li, J. Xiong, H. Song, S. Liu, Y. Huang, Y. Huang, G. I. N. Waterhouse, Z. Wang, Y. Mao and Z. Liang, *et al.*, *Sep. Purif. Technol.*, 2024, **341**, 126817.
111 L. Wang, Z. Zhang, Q. Han, Y. Liu, J. Zhong, J. Chen, J. Huang, H. She and Q. Wang, *Appl. Surf. Sci.*, 2022, **584**, 152645.
112 Y. Meng, L. Zhang, H. Jiu, Q. Zhang, H. Zhang, W. Ren, Y. Sun and D. Li, *Mater. Sci. Semicond. Process.*, 2019, **95**, 35–41.
113 F. Dai, M. Zhang, Q. Chen, M. Mi, Z. Li, J. Han, J. Xing, S. Feng and L. Wang, *Appl. Catal., B*, 2023, **336**, 122934.
114 R. Manna, G. Bhattacharya, S. Raj and A. N. Samanta, *J. Environ. Chem. Eng.*, 2024, **12**, 111722.
115 Y.-J. Wang, B. He, D. Ma, R. Li, Y. Xie and J.-R. Li, *Chem. Eng. J.*, 2023, **467**, 143329.
116 X. Yuan, Q. Mu, S. Xue, Y. Su, Y. Zhu, H. Sun, Z. Deng and Y. Peng, *J. Energy Chem.*, 2021, **60**, 202–208.
117 J. Becerra, D.-T. Nguyen, V.-N. Gopalakrishnan and T.-O. Do, *ACS Appl. Energy Mater.*, 2020, **3**, 7659–7665.
118 R. Manna, G. Bhattacharya, P. Sardar, S. Rahut and A. N. Samanta, *Renewable Energy*, 2024, **229**, 120752.
119 K. Qin, Q. Zhao, H. Yu, X. Xia, J. Li, S. He, L. Wei and T. An, *Environ. Res.*, 2021, **199**, 111360.
120 Y. Li, Y. Fu and M. Zhu, *Appl. Catal., B*, 2020, **260**, 118149.
121 X. Chen, J. Yao, B. Xia, J. Gan, N. Gao and Z. Zhang, *J. Hazard. Mater.*, 2020, **383**, 121220.
122 P. Garg, N. Dhingra, P. Attri, G. Yadav, M. Chauhan and G. R. Chaudhary, *Langmuir*, 2025, **41**(36), 24202–24213.
123 X. Quan, Y. Chen, L. Yin, W. Zuo, Y. Tian and J. Zhang, *ACS Appl. Mater. Interfaces*, 2024, **16**, 34973–34987.
124 F. Wu, C. Zhou, G. Tai, Y. Ma, X. Yang, Y. Pan, J. Han, W. Xing and G. Wu, *ACS Appl. Nano Mater.*, 2023, **6**, 17814–17825.
125 M. Pannerselvam, V. Siva, A. Murugan, A. S. Shameem, T. Bavani, S. Jhelai, S. Shanmugan, I. H. S. Ali and K. Kannan, *Nanomaterials*, 2025, **15**, 545.
126 W. Hou, Y. Huang and X. Liu, *Catal. Lett.*, 2020, **150**, 3017–3022.
127 H. B. Truong, G. Dastgeer, I. Zulfiqar, A. S. Alarifi, M. Kim, Y.-S. Seo and I. Rabani, *J. Mater. Sci.*, 2024, **59**, 18428–18445.
128 S. Sadiq, I. Khan, M. Humayun, P. Wu, A. Khan, S. Khan, A. Khan, S. Khan, A. F. Alanazi and M. Bououdina, *ACS Omega*, 2023, **8**, 49244–49258.
129 I. B. de S. Will, J. E. F. de Moraes, A. C. S. C. Teixeira, R. Guardani and C. A. O. do Nascimento, *Sep. Purif. Technol.*, 2004, **34**, 51–57.
130 S. Bustos-Guadarrama, A. Nieto-Maldonado, L. Z. Flores-López, H. Espinoza-Gomez and G. Alonso-Nuñez, *J. Taiwan Inst. Chem. Eng.*, 2023, **142**, 104663.
131 N. T. Tran and M. K. Nguyen, *et al.*, *J. Solid State Chem.*, 2021, **300**, 122287.
132 X. Li, S. Raza and C. Liu, *J. Taiwan Inst. Chem. Eng.*, 2021, **120**, 368–380.
133 W. Guan, X. Gao, G. Ji, Y. Xing, C. Du and Z. Liu, *J. Solid State Chem.*, 2017, **255**, 150–156.
134 Z. Wang, B. Wen, J. Zhou, X. Zhao, X. Zhang and Z. Su, *Materials*, 2022, **15**, 7683.
135 M. Shahsavari, M. Sheikhshoaei and S. Y. Ebrahimipour, *Water, Air, Soil Pollut.*, 2025, **236**, 397.
136 M. A. Nazir, O. P. Kumar, R. Ali, M. D. Hussain, S. Ullah, A. Rauf, A. M. El-Sherbeeny and S. S. A. Shah, *et al.*, *Korean J. Chem. Eng.*, 2025, **42**, 547–561.